PREPRINT (https://doi.org/10.1016/j.tust.2023.105446)
Ouyang, Zheng, Patmanidis, Naito, Quiel, Mooney - Tunnelling and Underground Space Technology

Full-Scale Testing of Precast Tunnel Lining Segments Under Thrust Jack Loading: Design Limits and Ultimate Response

Ziyan Ouyang, Haotian Zheng, Constantine Patmanidis, Clay Naito, Spencer Quiel, Michael Mooney

ABSTRACT

In modern practice, precast segmental tunnel linings are typically installed via a tunnel boring machine (TBM), which advances by thrusting against the previously installed segmental ring. The forces applied through the thrust jack pads can induce significant bursting and spalling tensile stresses and strains in the segment, and improperly designed segments can suffer from cracking as a result. An experimental study has been conducted to evaluate the progression of damage from initial cracking to ultimate capacity for full-scale precast tunnel liner segments under thrust jack loading. The baseline segment design is composed of steel fiber reinforced concrete (SFRC), and the impact of supplemental conventional steel bar reinforcement and load application eccentricity were also investigated. Six full-scale tests were performed with a thrust jack load per pad up to 22.2 MN (which is ~3.8 times the maximum expected installation thrust force). At the maximum expected thrust jack load during installation (5.78 MN per pad), the segments were virtually undamaged, and hairline cracking initiated between the load pads on only one test. At the TBM's ultimate jacking capacity (9.55 MN per pad) surface cracking was observed between and under the load pads; however, the crack width remained below 0.2 mm for all specimens. The formation of cracking limit states was accurately predicted by pre-test linear and nonlinear finite element (FE) models. At overload conditions, the baseline SFRC-only segment exhibited a radial bursting failure. The inclusion of supplemental conventional reinforcement does not reduce the level of cracking damage or strain development below the TBM's ultimate jacking capacity; however, at overload conditions, the supplemental reinforcement mitigates cracking and prevents a radial bursting failure at 20.3 MN per pad. A load eccentricity of 38 mm towards the extrados surface increased the transverse strain and the formation of transverse cracking at a lower load level.

KEYWORDS: precast segmental tunnel liner; thrust jacking load; tunnel boring machine; steel fiber reinforced concrete; tensile cracking limit states; finite element modeling

1. Introduction

Segmental precast concrete tunnel lining (PCTL) and TBMs have been increasingly adopted for modern tunnel construction to enable rapid construction in various geological conditions. For tunnels constructed using a standard TBM approach, circumferential PCTL rings provide both structural integrity to the bored tunnel cavity and a support against which the TBM can thrust forward. TBM thrust jacks push against the leading edge of previously installed PCTL segments at discrete pad locations during the boring process. Once adequate forward progress is achieved, a new ring of segments is installed via a segment erector. The segments are precast with a curved rectangular or parallelogram shape, and a trapezoidal key segment used to lock each ring into place. Typically, the number of segments ranges from 5 to 6 for transit tunnels with 6 to 7 m diameters, and 12 or more for larger roadway tunnels with diameters over 12 m.

Forward movement of the TBM can apply very high bearing forces (i.e. thrust jack load) to the exposed circumferential joints of the precast segments (ACI Committee 544 2016a). In many cases, thrust jack load during the tunnel's construction is the most significant load case for the design of these segments (Bakhshi and Nasri 2014) and can range from 1 to 6 MN per thrust jack pad depending on the tunnel diameter, thrust jack pad layout, and ground conditions (ACI Committee 544 2016a; Groeneweg 2007).

In design, stresses induced by thrust jack loads can be approximated using existing analytical expressions that were developed for estimating anchorage zone stresses in post-tensioned prestressed beams (Breen et al. 1994; Iyengar 1962). Studies have examined the accuracy of these approaches for estimating the thrust-induced stresses in a tunnel liner (Bakhshi and Nasri 2014; Conforti et al. 2016; Groeneweg 2007), which has led to the development of design guidelines per the American Concrete Institute (ACI Committee 544 2016b) and the International Tunneling and Underground Space Association (ITA Working Group 2 2019).

The use of finite element (FE) analyses is also recommended as an acceptable approach by ACI 544.7R-16 for determination of service state load conditions (ACI Committee 544 2016a).

To improve the durability of the tunnel during its operational life, PCTL segments are designed to incur minimal damage during installation. The segments and load pads are therefore sized to minimize the potential for tensile crack formation. As a result of the thrust force, tensile stresses and strains are expected to form in three general regions of the segment, as shown in Figure 1: (1) between the load pads (leading to transverse spalling cracks), (2) under the load pads in the transverse direction (due to transverse bursting cracks), and (3) within the body of the segment under the load pads in the radial direction (due to radial bursting cracks). Transverse bursting cracks can develop through the segment thickness and are usually observable on either the intrados or extrados surface of the segment. Radial bursting cracks are expected to form within the segment and therefore cannot be visually identified during construction or service.

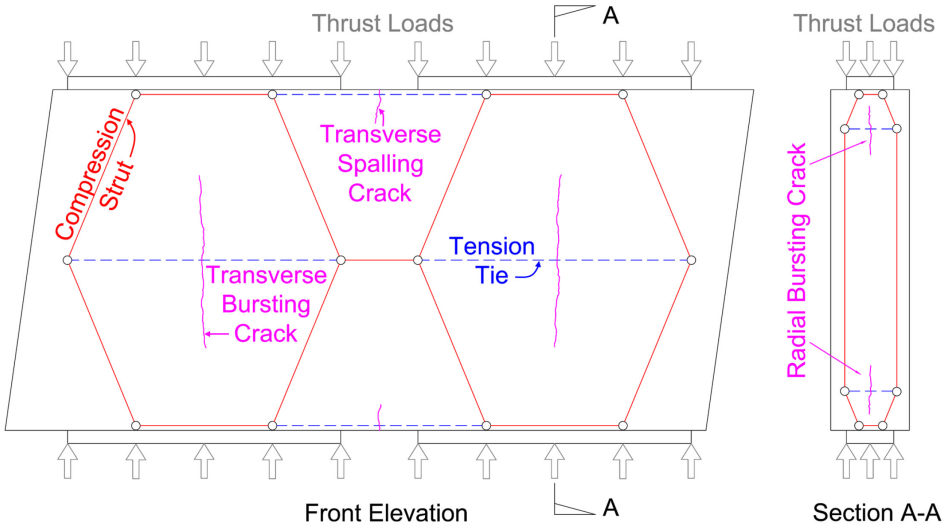

Figure 1: Simplified load transfer and potential crack formation in representative PCTL segment

Serviceability performance limits for PCTL segments under thrust jack loading are often tied to the formation and magnitude of cracks in the segment. The AASHTO LRFD Road Tunnel Design and Construction Guide specifies that crack widths shall be less than or equal to 0.2 mm (0.008 in.) to meet serviceability requirements of tunnel structures (AASHTO 2017). The same requirements can be found in DAUB Recommendation for the design, production and installation of segmental rings (German Tunnelling

Committee 2013). Since many segment geometries are sized to minimize crack formation under maximum expected thrust jack load, ultimate strength limit state is therefore rarely a design objective. To minimize crack size and limit crack propagation, fiber reinforced concrete (FRC) has been widely adopted for tunnel liners. Steel fiber reinforced concrete (SFRC) has emerged as one of the most common structural materials for tunnel segment fabrication in current practice (Winterberg and Clarke 2021).

Several previous studies (Abbas 2014; Caratelli et al. 2011; Hilar et al. 2012) have demonstrated that PCTL segments constructed from SFRC and RC can provide similar performance under thrust jack load; however, testing has shown that SFRC exhibits smaller distributed cracks while RC typically develops fewer but larger cracks (Beňo and Hilar 2013), which is undesirable from a durability perspective. Additional studies have shown that the addition of polypropylene fibers (PP) to a segment with conventional steel reinforcement can also produce a more distributed formation of smaller cracks (and thus better residual serviceability) after being subjected to relatively high thrust jack load levels (Conforti et al. 2017, 2019; Winterberg and Clarke 2021). To date, however, none of the available literature has experimentally examined the addition of steel fibers to a conventionally reinforced PCTL segment.

When the centerline of the thrust jack pads is not aligned with that of the bearing surface of the segment's circumferential joint, the resulting eccentricity can increase transverse crack formation at a given thrust jack load. In addition, due to reduced contact area between the thrust jack pad and the bearing surface, eccentric loading can cause higher radial bursting stress and strain formation, leading to unobservable internal damage. Previous numerical studies have shown that such an eccentricity in the segment's radial direction can cause crack formation at lower thrust jack load and ultimately produce larger crack sizes (Burgers et al. 2007; Krahl et al. 2021; Nogales and de la Fuente 2020; Trabucchi et al. 2021). ACI 544.7R-16 therefore suggests that the potential eccentricity of the thrust jack load in radial direction should be considered in design. If no specific value has been provided for the particular TBM system, a generic 30-mm radial eccentricity should be considered in both the intrados and extrados directions (ACI Committee

544 2016a). The impact of these eccentricities on realistically curved PCTL segments has not yet been evaluated in large scale experiments.

For this study, six tests were performed to apply thrust jack load on full-scale PCTL SFRC segments used for a U.S. roadway tunnel. Double-pad load tests were performed to simulate the loading conditions used during TBM tunnel construction, and single-pad load tests were performed to evaluate the ultimate capacity of the segments. The segment geometry and thrust jack load magnitudes applied in these tests (up to 22.2 MN for a single pad thrust jack load) is significantly higher than that used in past experimental programs, which commonly ranged from only 1.1 MN to a maximum of 9.3 MN (Beňo and Hilar 2013; Caratelli et al. 2011). The results are evaluated against the aforementioned AASHTO service crack size criterion of 0.2 mm as well as numerical predictions from pre-test FE analysis.

This paper examines experimentally for the first time the influence of supplementary steel reinforcing bars in combination with SFRC in precast tunnel segments during TBM operations. The accuracy of elastic and nonlinear FE analysis approaches in predicting serviceability limits for thrust jack loading on SFRC segments are also demonstrated in detail.

2. Precast Segment Properties

The SFRC segments for this study were obtained from a tunnel project currently under construction in the U.S. The hybrid segments which also included supplemental steel reinforcing bars were specially fabricated for this project using the same overall geometry and SFRC mix design, at the same fabrication site. The tunnel has an external diameter of 12.8 m, an internal diameter of 11.9 m, and resulting wall thickness of 457 mm. Each tunnel lining ring consists of ten circumferential segments. Segments in this study have an 8° longitudinal joint skew to facilitate the tunnel's longitudinal alignment, as shown in Figure 3. Each ring assembly consists of ten segments, including eight curved parallelogram segments, one large curved trapezoidal segment, and one curved trapezoidal key segment (highlighted in red). The segment lengths in

the longitudinal tunnel direction range from 1.93 m to 2.03 m, and widths in the circumferential (i.e. transverse) direction are approximately 4.09 m for the larger segments and 1.96 m for the key segments.

The TBM thrust jack loads are applied at nineteen thrust pad locations distributed around the circumference of the tunnel as shown in Figure 2 and Figure 3. The nine larger segments are subjected to two thrust jack pad loads, and the smaller keys segment is only subjected to one. The segments are detailed to ensure linear force transfer along the longitudinal direction of the tunnel. This is accomplished with the addition of a 4.0 mm raised region on the front and rear circumferential joint of each segment as shown in Figure 2 and Figure 3. The load from the thrust jack pad is transmitted linearly to the preceding ring segments along the longitudinal direction of the tunnel. The rotational offset of each ring is arranged so the elevated portion of the previous ring aligns with the line of force from the thrust jacks as illustrated in Figure 2.

Thrust jack load is applied to each pad by two hydraulic jacks, which together can apply a maximum force of 9.55 MN per pad (referred to herein as the “maximum jacking capacity per pad”). Based on the geotechnical profile for this particular tunnel alignment, the expected maximum thrust demand from the TBM during construction is 5.78 MN per pad. Note that the maximum expected thrust jack load and the maximum jacking capacity load levels are used in the experimental program as key observation points to assess performance.

The hydraulically applied thrust jack forces are distributed to the segment through a 120-mm thick steel plate and a 30-mm thick polytetrafluoroethylene (PTFE) pad, inserted between the steel plate and the concrete to reduce the development of localized lateral shear stress. The thrust jack pads are curved to align with the tunnel circumference and are dimensioned to be 1600-mm long by 276-mm wide (see Figure 2 and Figure 3). The centerline of the hydraulic jacks and the centerline of the concrete segment are concentric. The contact area, however, is radially offset by 4.8 mm toward the intrados surface due to the presence of a waterproofing gasket near the extrados surface as shown in Figure 2.

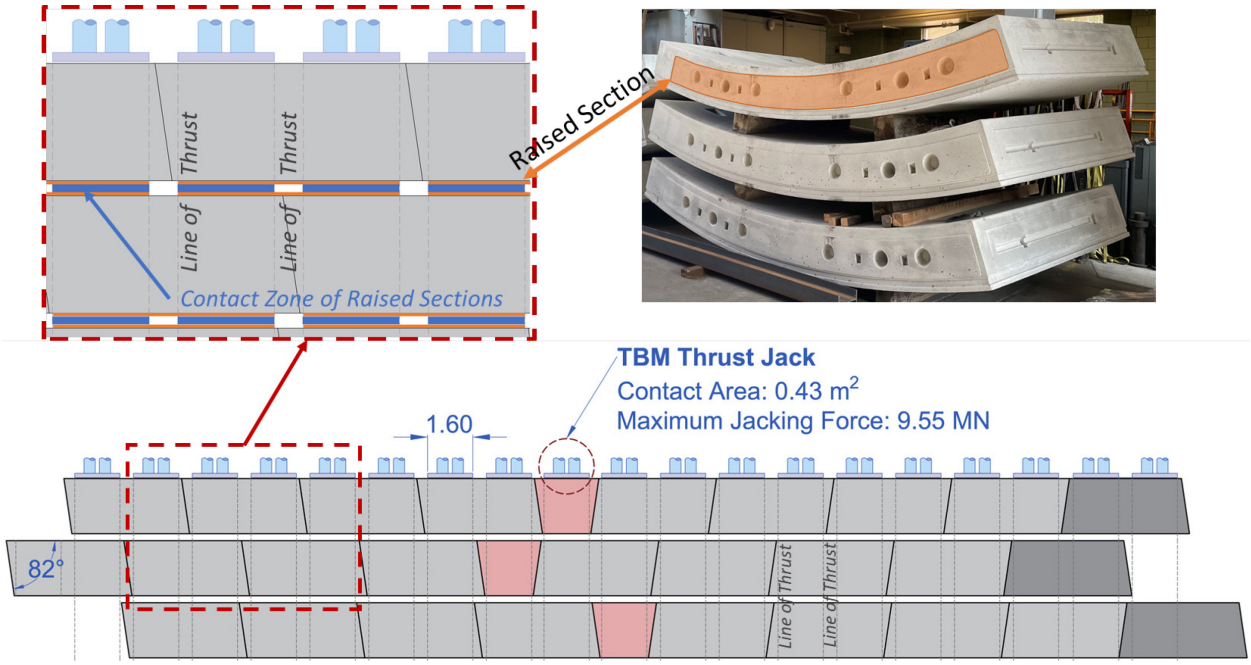

Figure 2: Illustration of lining segments and ring configuration (shown unwrapped) for the prototype tunnel

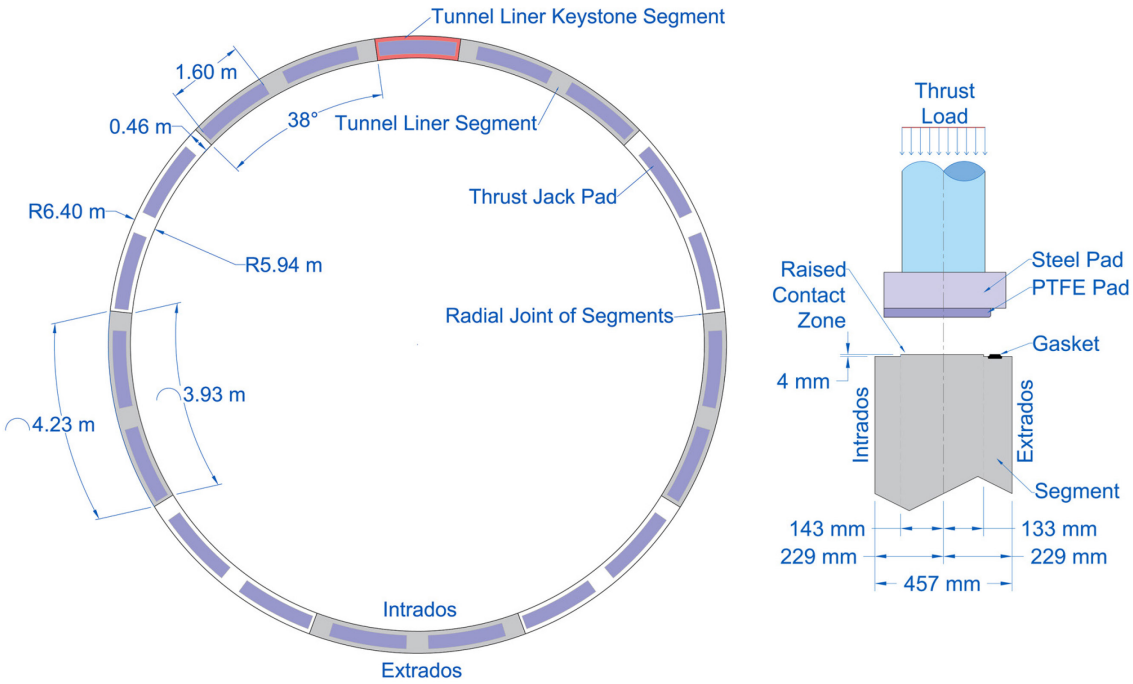

Figure 3: Illustration of TBM thrust jacking loads applied to ring bearing area

2.1. Steel Fiber Reinforced Concrete Properties

All segments for the tunnel project and the specimens in this study utilize an SFRC mix designed to provide the requisite compressive strength and adequate tensile cracking and post-cracking performance to enable the elimination of conventional reinforcing bars. Table 1 summarizes the mix proportions as well as the plastic properties from a typical sample. The mix utilizes Type I/II Portland cement with the following replacements by weight: 40% slag replacement and 5.33% silica fume. Dramix 4D steel fibers, which conform to ASTM A820, EN 14889-1 and ISO Class A (ASTM Standard A820-16 2016; CEN 2006; ISO 2013), were added at 0.51% by volume. Each fiber has a length of 60 mm and a diameter of 0.75 mm, and both ends are crinkled for enhanced bond with the concrete. Each fiber is composed of cold drawn steel wire has a nominal tensile strength of 1800 MPa, an elastic modulus of 200 GPa, and an ultimate strain of 8000 $\mu\varepsilon$.

Table 1: SFRC mix design

Constituent	Description	Values
Cementitious	Cement I/II	243.2 kg/m^3
	Grade 120 GBFS (Granulated Blast Furnace Slag)	178.0 kg/m^3
	Sikacrete 950 DP Silica Fume	23.7 kg/m^3
	Total Cementitious	445.0 kg/m^3
Aggregate	Coarse Aggregate #8	949.2 kg/m^3
	Fine Aggregate	688.2 kg/m^3
Steel Fiber	Dramix 4D Fiber	38.6 kg/m^3
Water	Water	155.7 kg/m^3
	Water/Cement Ratio	0.350
Design Air	Entrained	6.0%
Superplasticizer	Sika ViscoCrete 6100	4.7 kg/m
Air Entraining Admixture	Sika AEA 14	0.8 kg/m^3
Sample Measured Plastic Properties	Slump	2544 mm
	Air Content	5.5%
	Concrete Temperature	20.0 °C
	Ambient Temperature	19.4 °C
	Unit Weight	2337 kg/m^3

The SFRC compressive strength and elastic modulus were assessed in accordance with ASTM C39 and C469 (ASTM Standard C39-20 2020; ASTM Standard C469-14 2014), respectively. Uniaxial tensile properties can be determined using inverse analysis of small-scale flexural beam test results (ACI Committee 544 2016a) or through a direct tension test approach (Graybeal and Baby 2013). For the SFRC

mix in this study, splitting tensile strength and the crack mouth opening displacement (CMOD) were determined in accordance with ASTM C496 and EN 14561 (ASTM Standard C496-17 2017; CEN 2005), respectively. Table 2 summarizes the properties measured by the precast fabricator when the specimens were cast as well as those measured by the research team prior to thrust jack load. A total of 12 CMOD tests conducted by the precast fabricator are plotted in Figure 4(a), in which the average curve is represented as a single thick black line. Note that the contract documents for the tunnel project defined performance metrics at crack mouth opening displacement values of 1.1 and 3.5 mm as stated. As shown in Table 2, all average properties met the required minimum values for the design of these segments. Note that the standard deviation in compressive strength is greater at late ages due to the use of cores; all compressive strength tests exceeded the minimum requirement. As noted in Table 2 and Figure 4, while the CMOD data met the tension requirements on average, two of the twelve tests at CMOD of 1.1 mm failed below the minimum required value of 4.82 MPa and all of the CMOD 3.5 mm tests exceeded the requirement. This was deemed acceptable for the project.

Table 2: SFRC structural material properties

Property	Required Min. Value [MPa]	Fabricator Measured Value [MPa] (age in days)	Measured from Cores [MPa] (age in days)
Elastic Modulus	34000 short term 20000 long term	Not available	30940+/-1550 (610 to 723)
Poisson's Ratio	Not Specified	Not Available	0.196+/-0.0217 (610 to 723)
Compressive Strength	52	65.6+/-5.2 (28)	64.3+/-9.5 (610 to 723)
Splitting Tensile Strength	4.2	7.34+/-0.17 (28)	7.05+/-0.85 (610 to 709)
CMOD Peak Strength	4.2	7.12+/-0.32	Not Applicable
CMOD 0.5 mm	Not Specified	4.57+/-0.83	Not Applicable
CMOD 1.1 mm	4.82	5.83+/-1.32	Not Applicable
CMOD 3.5 mm	3.45	6.28+/-1.30	Not Applicable

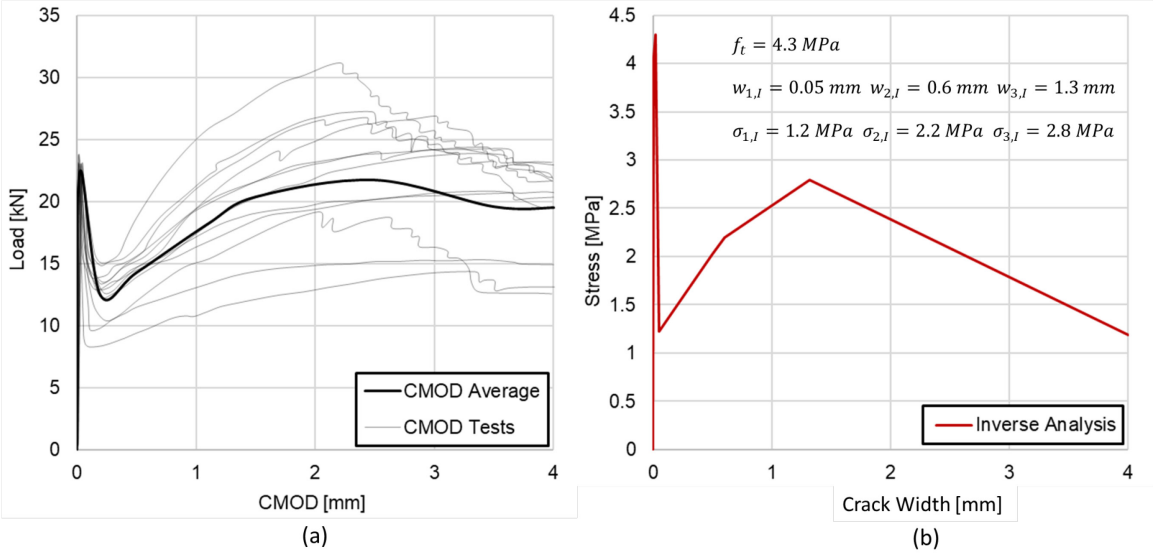

Figure 4: Tensile data: (a) measured CMOD load-displacement, and (b) inverse analysis stress-crack results

The serviceability performance of the segments to thrust jack loading was assessed relative to the formation of cracks in the SFRC material. This is determined through visual inspection where possible and through the use of strain gages. The determination of a tensile strain limit at which cracking occurs is thus critical to assess performance of the segments under load. The strain at cracking is calculated by dividing the tensile strength by the measured average elastic modulus noted in Table 2. Uniaxial tensile strength can be estimated using three approaches, the results of which would be expected to bound the actual cracking strain in the segments. The first approach calculates the tension strain limit using the measured split cylinder tension strength. The loading condition for a split cylinder test does not generate a uniform tension stress profile, thus this approach is considered to provide only an approximate upper bound estimate (Abrishambaf et al. 2015; Shen et al. 2020).

The second approach consists of an inverse analysis of the CMOD data (Stephen et al. 2019). Specifically, the approach is based on a closed-form solution that relates the multi-linear stress-crack opening to the load-CMOD curve. A tetra-linear model of the stress-crack opening curve was computed as shown in Figure 4b with the crack opening values or 0.05, 0.60, and 1.3 mm chosen based on recommendations by Stephen

et al. 2019. The analytical model is based on the concept of a non-linear hinge formation in a three-point bending test (Olesen 2001). The nonlinear hinge is placed at midspan with length equal to half the beam depth. The hinge is modeled as layers of spring elements with their behavior governed by the tensile constitutive relation of the concrete. The parameters of the SFRC stress-crack width curve were found by fitting the load-CMOD curve obtained for each EN14651 test (CEN 2005) on the SFRC (Figure 4b) and averaging the values. The solid black line shows the load-CMOD curve using the average values of inverted parameters from individual tests, and the red line shows the stress-crack width relationship using the average inverse parameters. An average peak tensile strength, f_l, of 4.3 MPa is estimated via the inverse analysis. Dividing the tensile strength by the elastic modulus results in a strain of 139 $\mu\varepsilon$. The estimated average residual tensile strengths, $\sigma_{i,I}$, corresponding to crack widths, $w_{i,I}$, of 0.05, 0.6, and 1.3 mm are 1.2, 2.2, and 2.8 MPa, respectively. The tensile strain values across the crack plane are computed using the sum of the elastic deformation of the strip and the magnitude of the crack opening (Stephen et al. 2019). The tensile constitutive properties are presented in the numerical analysis section.

The third approach, proposed by RILEM (RILEM TC 162-TDF 2003) and recommended by ACI (ACI Committee 544 2016b), suggests that the residual flexural strength corresponding to a crack mouth opening of 0.5 mm should be used to determine the serviceability limit state. The approach converts the measured flexural tensile strength of an SFRC beam to a uniaxial tensile strength using Equation 1:

$$f_t = C_1(1.6 - d)f_{tm,fl} \quad \text{Equation 1}$$

where d is the depth of the beam's cross-section, and $f_{tm,fl}$ is the average value of the measured peak flexural tensile strength before cracking (7.12 MPa). C_1 is assumed to be 0.52 (Barros et al. 2004), and the resulting estimated uniaxial tensile strength is therefore 5.46 MPa. The uniaxial residual strength, $f_{t,r}$, and corresponding strain, $\varepsilon_{t,r}$, at 0.5 mm crack mouth opening can then be expressed according to equations 2 and 3.

$$f_{t,r} = 0.45 \cdot f_{R,1} \cdot \kappa_h \quad \text{Equation 2}$$

$$\varepsilon_{t,r} = \frac{f_t}{E_c} + 0.001 \quad \text{Equation 3}$$

where $f_{R,1}$ is the 0.5 mm post-crack residual flexural strength (4.57 MPa); E_c is the elastic modulus of SFRC; and κ_h is the size factor of the specimens used for beam flexural tests (equal to 1 for a beam specimen with 150-mm depth and a 25-mm deep notch at the tension face).

As summarized in Table 3, the uniaxial tensile strain limit ranges from 139 to 237 $\mu\varepsilon$, with the lower bound from the inverse analysis approach and the upper bound from the split cylinder data. This range from the lower limit, $\varepsilon_{t,l}$, to upper limit, $\varepsilon_{t,u}$, will be used as the basis for evaluating the strain data acquired from thrust jack load testing of the full-scale segments. The strain at 0.5 mm post-crack residual uniaxial strength is computed from the inverse analysis to be 6667 $\mu\varepsilon$. A strain of 1066 $\mu\varepsilon$ at the 0.5 mm post crack displacement is determined using the RILEM approach and is calculated using Equation 3.

Table 3: Tensile stress and strain limits of SFRC

Approach	Strength Type	Stress Limit (MPa)	Strain Limit ($\mu\varepsilon$)
Splitting Tension Tests	Splitting Tensile Strength, $f_{t,sp}$	7.34	237
CMOD Tests	Flexural Tensile Strength, $f_{tm,fl}$	7.12	230
	0.5 mm Post-Crack Residual Flexural Strength, $f_{R,1}$	4.57	N.A.
Inverse Analysis	Uniaxial Tensile Strength, $f_{t,i}$	4.30	139
	0.5 mm Post-Crack Residual Uniaxial Strength, $f_{t,r,i}$	2.03	6667
RILEM Approach	Uniaxial Tensile Strength, f_t	5.46	176
	0.5 mm Post-Crack Residual Uniaxial Strength, $f_{t,r}$	2.06	1066

2.2. Conventional Reinforcement for Hybrid Segments

The performance of the baseline SFRC segments is compared against that of hybrid segments for which carbon steel reinforcing bars are used in conjunction with the same SFRC mix. As shown in Figure 5, two rows of longitudinal bars are installed parallel to each joint face, and radial bars are included to provide confinement against bursting in the radial direction at these locations (thus forming a ladder pattern with longitudinal bars). All bars conform to ASTM A615 Grade 420 (ASTM Standard A615-18 2018) and have a standard cover of 51 mm per ACI 318 for reinforced concrete elements exposed to weather (ACI

Committee 318 2019). All contact points between bars are welded, as opposed to hooked, to ensure full development due to the limited space within the segment. Tensile testing on samples of the No. 19, 22, and 25 reinforcing bars that were used in the hybrid specimens produced an average yield strength of 412.5, 415.0 and 451.0 MPa, and average tensile strengths of 627.6, 585.9, and 643.7 MPa, respectively.

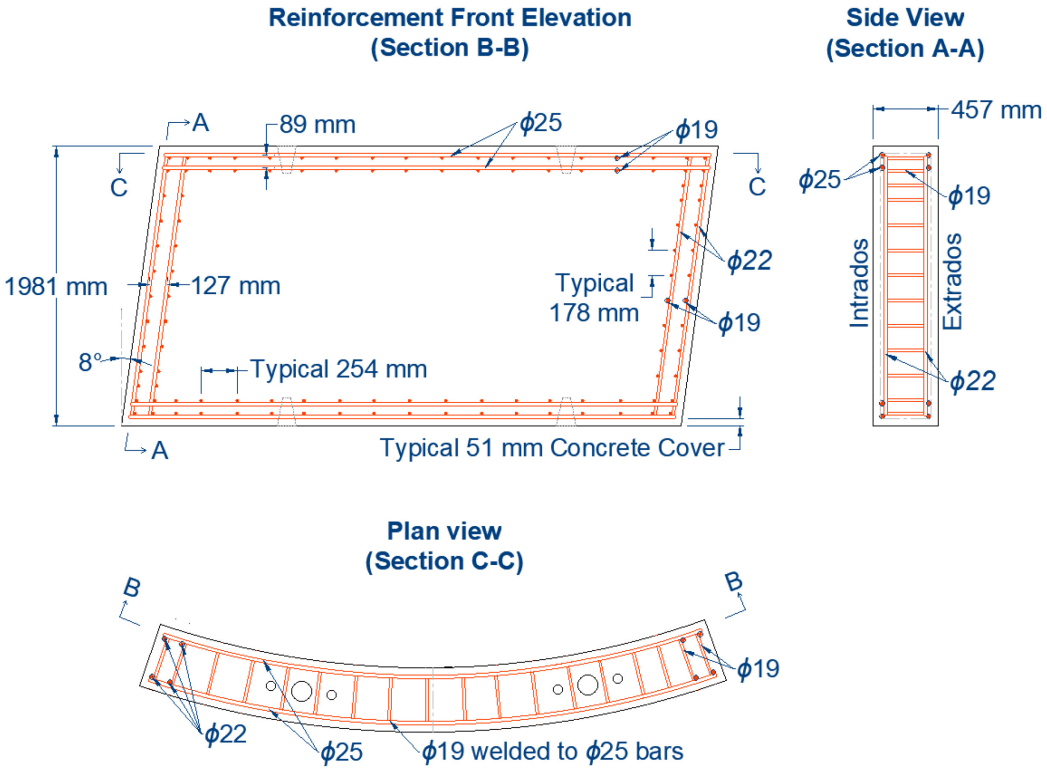

Figure 5: Layout and detailing for steel reinforcing bars in the hybrid segments

2.3. Numerical Predictions of Expected Response

Four 3D FE models were developed using Abaqus CAE/Standard (Dassault Systèmes 2019) to predict the expected response of the unreinforced PCTL segments to thrust jack loading. The focus of the models is to examine the distribution of stresses and the achievement of cracking (e.g., the tensile concrete strength limits) rather than the ultimate response. Reinforcement is not directly modeled as the stress in the bars in the hybrid segments are low at these load levels. All models, summarized in Table 4, use the measured value of elastic modulus and Poisson's ratio (30,940 MPa and 0.196 per Table 2) as direct inputs. Model 1 has an elastic SFRC material model with thrust jack load applied in a concentric manner per Figure 3 (i.e.,

without eccentricity). Models 3 and 4 are duplicates of Model 1 but with the thrust jack load applied with a radial eccentricity of 51 mm towards the intrados and extrados surfaces, respectively. The 51-mm eccentricity value corresponds to an imperial unit of 2.0 inches which was recommended by the U.S. TBM manufacturer and tunnel designer for the segments in this study and is larger than the standard 30-mm value recommended by ACI 544-7R (ACI Committee 544 2016a).

Model 2 applies the same concentric thrust jack load as Model 1 but utilizes a nonlinear concrete damage plasticity (CDP) material model for the SFRC, based on the measured tensile material properties and the inverse analysis approach along with compressive properties based on *fib* MC-2010 (International Federation for Structural Concrete 2013). The measured value of compressive strength (65.6 MPa) and the uniaxial tension properties from inverse analysis of the CMOD test data were used as input for the nonlinear material in Model 2. The resulting constitutive stress-strain relationships for SFRC in Model 2 are plotted in Figure 6.

Table 4: Matrix of FE models used to predict the expected response of a single SFRC segment to thrust jack loading

Model No.	SFRC Material Model	Thrust jack load Application
1	Linear Elastic	Double Pad, Concentric
2	Nonlinear (see Figure 6)	Double Pad, Concentric
3	Linear Elastic	Double Pad, Eccentric at 51 mm towards Intrados
4	Linear Elastic	Double Pad, Eccentric at 51 mm towards Extrados

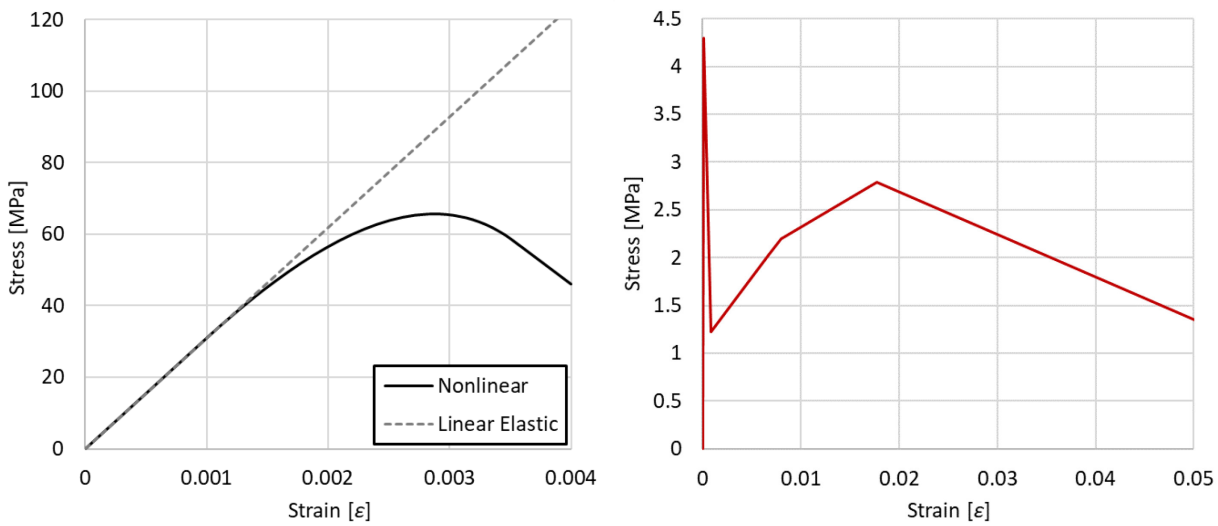

Figure 6: Nonlinear stress-strain relationships (left: compression, right: tension) used as input for Model 2

The FE models use C3D8R (reduced integration) solid elements with an average element mesh size of 38 mm (as determined via a preliminary convergence study). The highlighted areas at the bottom of the segment in Figure 7 are vertically restrained and have additional restraints in the horizontal plane that are marked with triangles. The horizontal restraints were needed to maintain static equilibrium and were applied in such a pattern as to not artificially over-restrain the supported faces. As shown in Figure 7, the thrust jack load application is idealized as a uniform pressure over the thrust jack pads per their footprint in Figure 2. This assumption is based on the fact that the 30 mm Teflon is mounted in the real system to a rigid 120 mm steel plate. The thrust jack load is increased monolithically to determine the load levels when the tensile strain limits are reached. To evaluate the impact of this simplification, a preliminary analysis of Model 1 was conducted in which a 30-mm thick Teflon pad (used by the actual TBM thrust jacks) was modeled on top of the highlighted loading zones in Figure 7 and then loaded with the same uniform pressure. The results of that analysis showed no substantial difference in stress distributions versus the simplified case with direct load application (which was therefore used for all subsequent analyses).

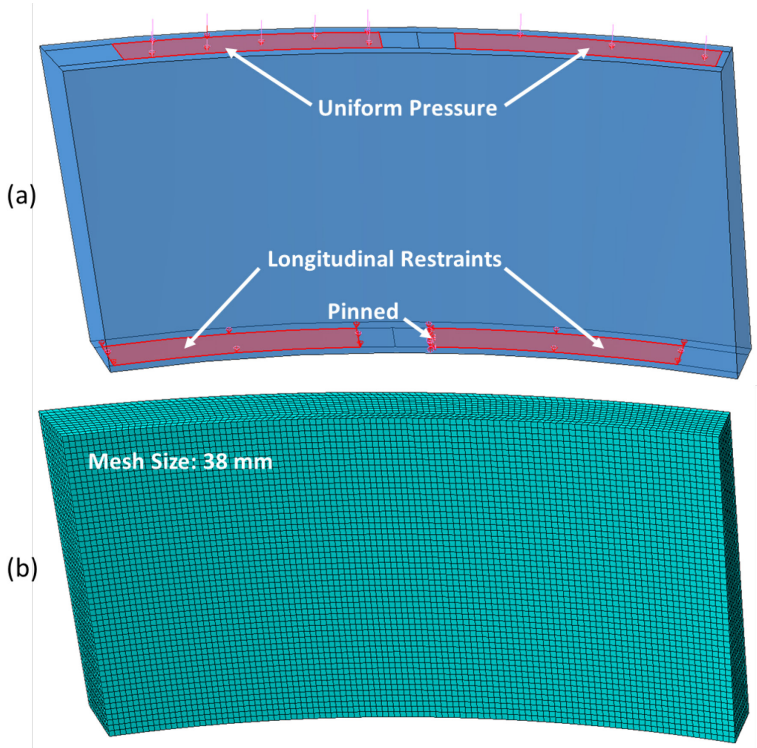

Figure 7: FE model setup: (a) loading and boundary conditions, and (b) mesh

The principal strains in the four models are compared to examine the impact of loading and constitutive modeling on the tensile strain development in the segments. The maximum principal strain contours from Model 1 are plotted in Figure 8, as well as the general locations where bursting and spalling tensile strains are developed due to thrust jack load. The results are illustrated in the post cracking regime with a load of 7.4 MN applied to each pad. The maximum principal strain is generally the larger value of transverse and radial bursting strains. The observed regions of elevated tensile strain correlate with the expected damage zones illustrated in Figure 1. The cross-section at the white dashed line in Figure 8 illustrates the radial bursting strain distribution within the segment thickness under the center of a load pad. The maximum transverse spalling strain forms between the load pads in the transverse (i.e. circumferential) direction. The maximum transverse bursting strain develops at the mid-width of the segment under the load pad, again along the transverse direction. The maximum radial bursting strain develops near the load pad at approximately 200 mm (less than half the 457 mm segment thickness) under the highlighted loading zone along the radial (i.e. thickness) direction. The maximum principal strain contours from the nonlinear Model 2 with 7.4 MN at each load pad are very similar to those shown for Model 1 in Figure 8 and are therefore not plotted for brevity.

The results of eccentric Model 3 are plotted in Figure 9; as expected, radial eccentricity toward the intrados causes longitudinal flexure in the segment resulting in an increase intrados compression and extrados tension. This increases the transverse bursting strain on the intrados face and reduces the transverse bursting strain on the extrados face. Similarly, eccentricity toward the extrados for Model 4 in Figure 10 decreases the strain in that area. The eccentricity also affects the distribution of transverse spalling strains, which marginally increase on the bearing side (i.e. bottom circumferential joint) for the intrados eccentricity and significantly increase on the loading side (i.e. top circumferential joint) for the extrados eccentricity. As would be expected, these results indicate that an eccentric thrust jack load application would likely result in earlier formation of transverse spalling cracks versus a concentric load.

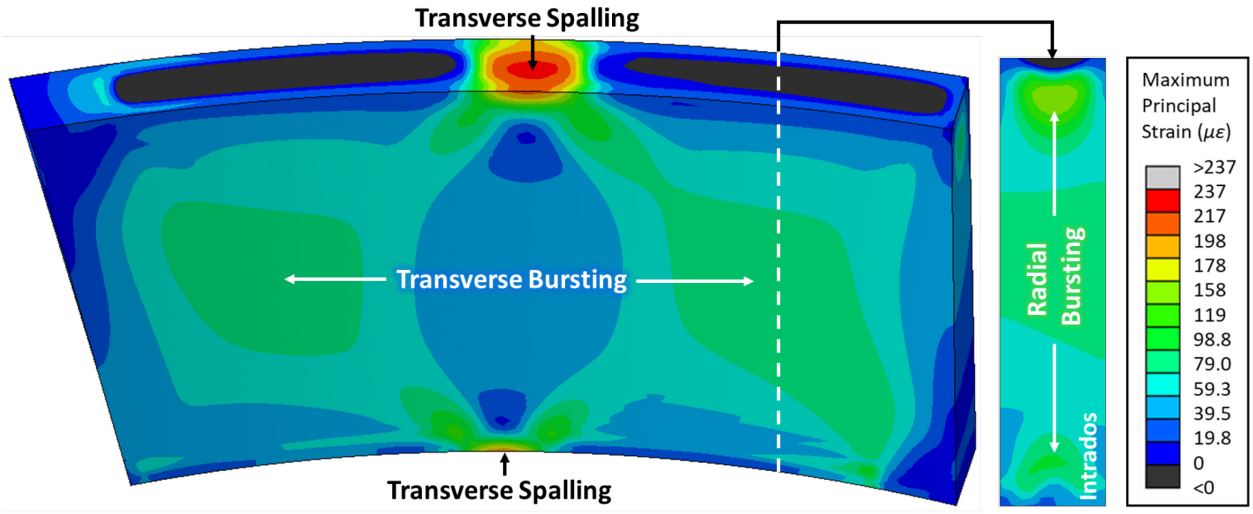

Figure 8: Maximum principal strain of Model 1 under 7.4 MN per pad

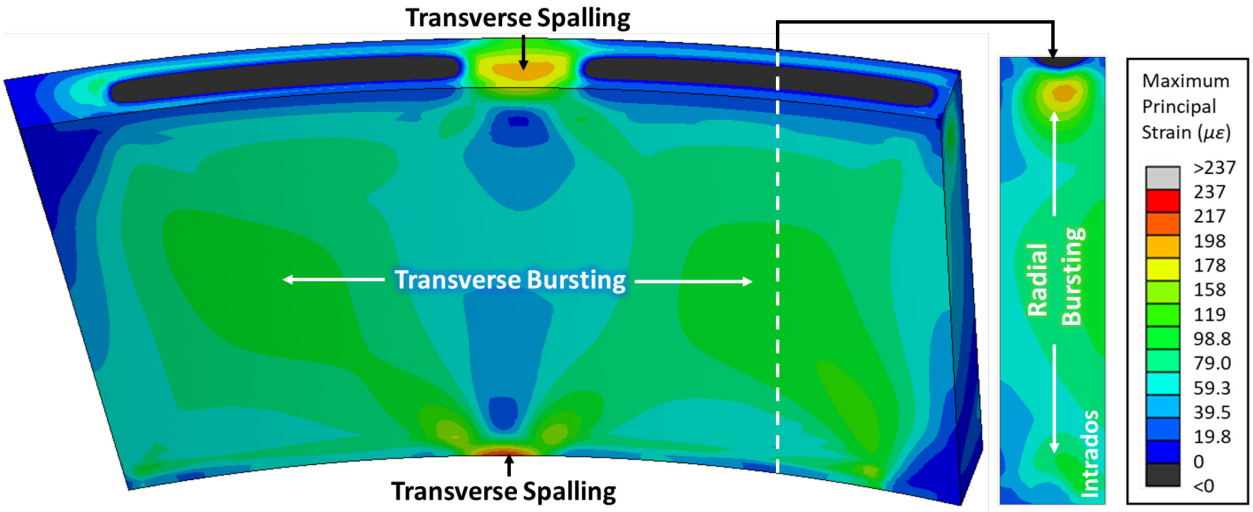

Figure 9: Maximum principal strain of Model 3 (51 mm intrados eccentricity) under 7.4 MN per pad

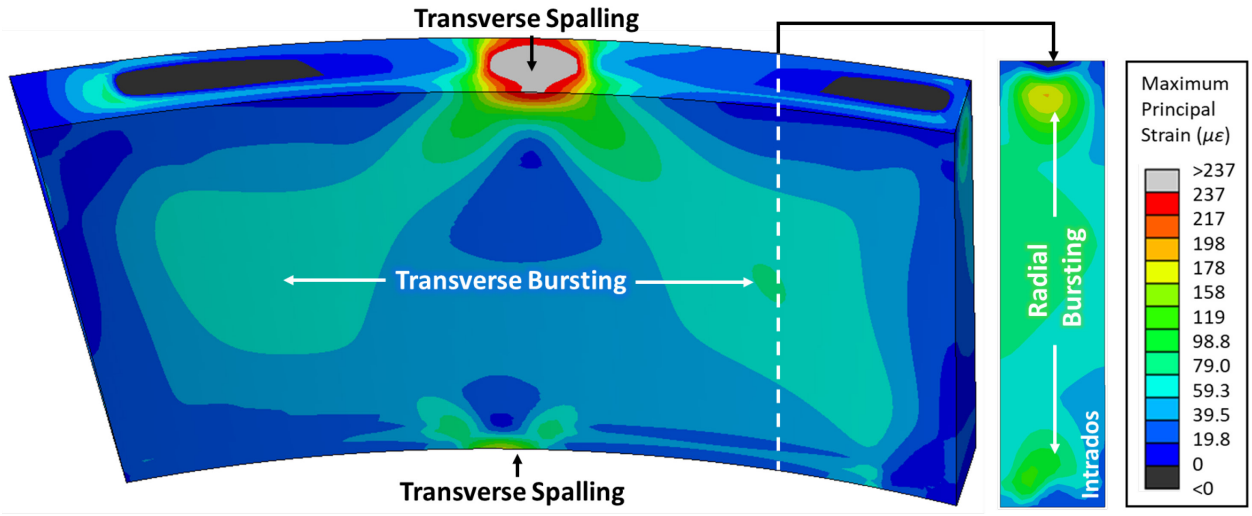

Figure 10: Maximum principal strain of Model 4 (51 mm extrados eccentricity) under 7.4 MN per pad

Tensile strain output from the FE models are used to determine the expected load level and the corresponding locations at which the segment would develop tensile cracking (compared against the lower and upper bound limits, $\varepsilon_{t,l}$ and $\varepsilon_{t,u}$, of 139 and 237 $\mu\varepsilon$ per Section 2.1). Since Models 1, 3 and 4 are elastic, it should be noted that the simulated tensile stress-strain response is not impacted by those limits and can continue to increase past the point at which a crack would realistically. Therefore, any results produced after the tensile limit is first reached at any location in the elastic model can accumulate error if the crack formation impacts the subsequent stress flow at escalating load levels. The results of elastic Model 1 at progressive states of cracking are therefore compared against those from the inelastic Model 2 to examine the impact of crack-induced tensile stress limitations on stress flow within the segment.

The total applied thrust forces needed to reach the tensile limits due to transverse spalling, transverse bursting, and radial bursting are summarized in Table 5. Transverse spalling cracks occur first for all models, followed by radial bursting and then by transverse bursting cracks. Recall that the inelastic Model 2 uses the concrete tensile constitutive properties defined in Figure 6, which is based on the lower bound tensile strain limit, $\varepsilon_{t,l}$. Consequently, no upper bound values are reported for Model 2. Therefore, the comparison that follows between all four models is predicated on the results in Table 5 for $\varepsilon_{t,l}$. Thrust pad

loads corresponding to the upper bound tensile strain limit, $\varepsilon_{t,u}$, are provided in Table 5 to establish an upper bound threshold against which the results of testing will be evaluated later in Section 4.

Table 5: Total thrust jack load per pad (MN) corresponding to tensile strain limits for each cracking mode in Figure 1

Case	Transverse Spalling		Radial Bursting		Transverse Bursting	
	$\varepsilon_{t,l}$	$\varepsilon_{t,u}$	$\varepsilon_{t,l}$	$\varepsilon_{t,u}$	$\varepsilon_{t,l}$	$\varepsilon_{t,u}$
Model 1	4.7	7.8	6.8	11.3	10.6	18.0
Model 2	4.7	N.A.	6.6	N.A.	10.6	N.A.
Model 3	4.2	7.3	5.4	9.3	8.9	15.6
Model 4	3.9	6.4	5.8	9.8	10.5	18.0

Results for Models 1 and 2 in Table 5 both indicate the first instance of cracking via transverse spalling per $\varepsilon_{t,l}$ at the same 4.7 MN thrust pad load. This result confirms the negligible influence of material nonlinearity at this load level. As the thrust jack load subsequently increases, the models continue to produce very similar results. Specifically, radial bursting per $\varepsilon_{t,l}$ is reached only 3% sooner in the inelastic Model 2, and both models reach transverse bursting per $\varepsilon_{t,l}$ at the same 10.6 MN load. These results indicate that tensile cracking had a nearly negligible impact on the stress flow in these segments, which have substantial size and can widely distribute stresses throughout the SFRC material around cracks. The SFRC material acts more like a continuum for tensile stress redistribution, as opposed to a conventionally reinforced segment without fibers which relies on its reinforcing bars to discretely resist post-cracking tension forces. The linear FE model can therefore provide a suitably accurate prediction of the location and thrust jack load at which tensile cracking occurs in these SFRC PCTL segments. Based on the analyses, nonlinear FE analysis is not necessary to determine the occurrence of radial bursting, transverse bursting and transverse spalling crack formation in tunnel liners subject to thrust loads.

As would be expected, results for Models 3 and 4 in Table 5 show that progressive tensile cracking at all three modes is reached at slightly lower thrust pad loads compared to Model 1 due to the additional flexural stresses induced by eccentric loading. Transverse spalling is more heavily impacted by the extrados

eccentricity, as Model 4 needs 17% less thrust jack load to reach this mode of tensile cracking per $\varepsilon_{t,l}$ than Model 1. Both radial and transverse bursting are more impacted by the intrados eccentricity in Model 3, again at ~17% less thrust jack load for both modes compared to Model 1. These results suggest that an expected upper bound thrust jack load eccentricity should be accounted for when linear FE models are used to design this type of PCTL segment.

3. Experimental Program

3.1. Specimen Matrix

The six experiments summarized in Table 6 were conducted on individual PCTL segments per the schematic in Figure 11, which was intended to emulate thrust jacking load from a TBM: three double pad tests and three single pad tests. A universal testing machine with 22.2-MN capacity was used to apply quasi-static loading at a rate of 0.300 MN/min, and loading was paused at multiple levels to observe and record crack formation. TBM thrust load application rates vary based on operation conditions, quasi static loading rates were conservatively used in the experimental program. It is expected that faster loading rates would result in concrete strength increase and less crack development. Cracking patterns and sizes were marked progressively through the loading history and documented. The double pad load tests were performed first and represented a conventional thrust jack loading condition with concentric load positioning. The results of these tests enable a direct comparison between the SFRC and hybrid reinforced segments (see Figure 5).

As will be shown later in Section 4, these tests exhibited a similar progressive onset of tensile cracking as the FE model results in Table 5; however, none of the double pad tests were able to surpass their ultimate resistance (i.e. “fail” due to a rapid loss of stiffness) due to the load capacity of the testing machine, which could apply 11.1 MN at each pad. Three additional tests were then performed with a single pad load, which is not typically representative of actual TBM installation process for these segments but could ensure that the ultimate load from a single pad would be reached. Two of the single pad tests used concentric loading, while the third used a 38 mm extrados eccentricity. Recall that the extrados eccentricity of Model 4

produced the earliest onset of the first tensile cracking via transverse spalling (see Table 5). The extrados direction for the third single pad test would therefore be expected to produce a conservative onset of the first instance of tensile cracking. This tested value is greater than the 30 mm recommended by AASHTO and less than the 51 mm recommended by the TBM system. This eccentricity was chosen to limit the bending moment reaction that would be imparted to the testing machine at the maximum load of 22.2 MN.

To emulate the TBM thrust jack pad load transfer, a 6.4 mm thick steel plate and a 3.2 mm thick PTFE sheet were sandwiched as a bearing pad between the spreader beam and the top of the concrete segment. At the bottom of the segment, a 6.4 mm thick steel shim was used to create a boundary condition similar to what would be provided by a preceding tunnel ring as shown in Figure 3. The dimensions of the steel pads and Teflon/PTFE sheets used in the experiment are shown in Figure 11. The physical arrangement of the loading system and segments within the universal testing machine are pictured in Figure 12.

The segments were procured from the actual tunnel construction effort and therefore considerably ranged in age when tested. As shown in Table 6, the segment age on the day of thrust jack load testing ranged from 199 to 673 days after casting; however, the compressive and tensile strengths of the concrete did not vary significantly from 28 to 709 days, as shown previously in Table 2. It should be noted that four total segments (two each for SFRC and hybrid) were tested in this program. One SFRC and two hybrid segments were used initially for double pad load tests – as will be discussed later in Section 4, these specimens only exhibited marginal observable tensile cracking when subjected to the 11.1 MN maximum pad load in this setup. The two hybrid segments were therefore reused for a second test under single pad loading to reach their ultimate response.

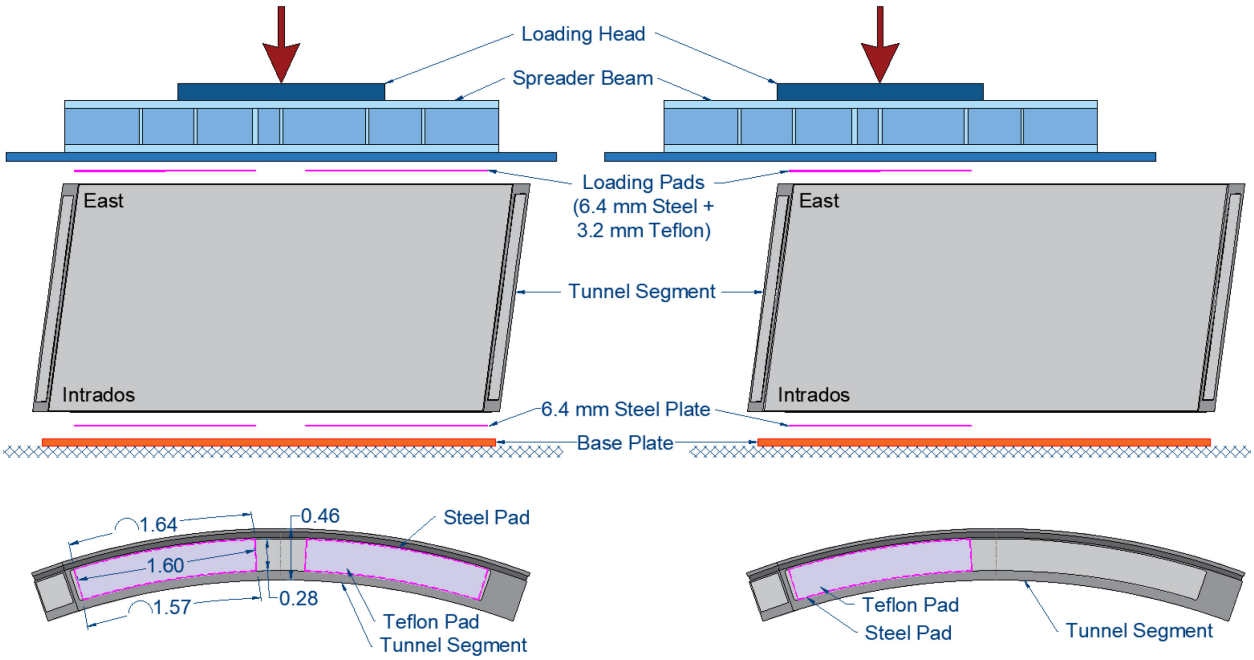

Figure 11: Configuration of double pad test (left) and single pad load test (right)

Table 6: Matrix of six thrust jack load tests, conducted on four total PCTL segments

Test ID*	Type	Loading Condition	Max Load	Age at Testing	Description
D-SC	SFRC	Double Pad, Concentric	11.1 MN	673 days	Serviceability Test for SFRC
D-HC	Hybrid	Double Pad, Concentric	11.1 MN	214 days	Serviceability Test for Hybrid Reinforcement
D-HC-2	Hybrid	Double Pad, Concentric	10.0 MN	199 days	Duplicate of Test D-HC
S-SC	SFRC	Single Pad, Concentric	20.3 MN	313 days	Ultimate Test for SFRC
S-HC	Hybrid	Single Pad, Concentric	22.2 MN	203 days	Ultimate Capacity Test for Previously Tested D-HC-2 Specimen
S-HE	Hybrid	Single Pad, Eccentric	22.2 MN	216 days	Ultimate Capacity Test for Previously Tested D-HC Specimen, with 38 mm Eccentricity to Extrados Surface

*D = double pad, S = single pad, SC = SFRC concentric, HC = hybrid concentric, HE = hybrid eccentric

Figure 12: Test setups for thrust jacking load testing

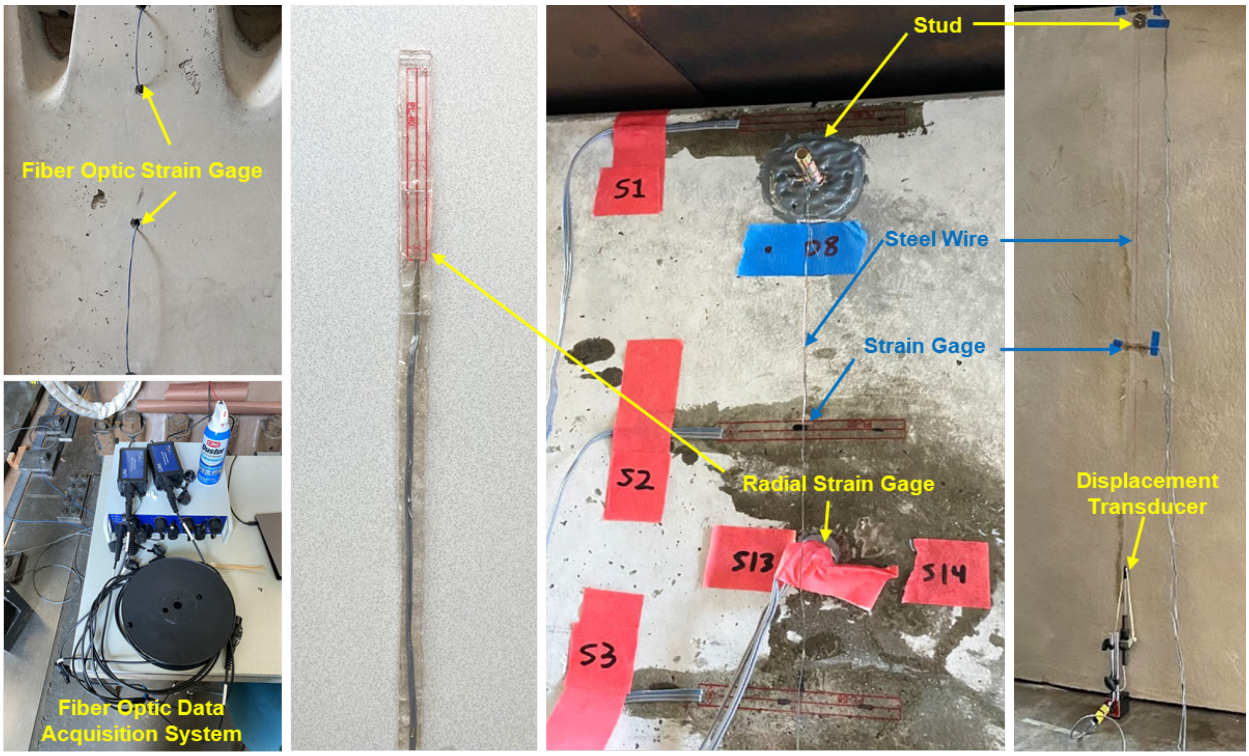

Figure 13: Segment instrumentation examples: fiber optic system, strain gage, radial strain gage, and displacement transducer

3.2. Instrumentation

All segments were instrumented with resistance-based strain gages and displacement transducers as shown in Figure 13. Displacement transducers were used to monitor the global position (i.e., movement along longitudinal, transverse and radial directions) of the segment during loading. The strain gage layout (illustrated in Figure 14) was informed by the strain distribution results from FE models (see Figure 8) to target noteworthy regions of response. Transverse strains were measured using surface mounted resistance-based gages. For the D-SC specimen, a strand of fiber optic strain gages was inserted through small holes which were then filled with hard epoxy to obtain a continuous measurement of radial strain through the segment thickness. For all other specimens, radial strains were measured using resistance-based gages placed into small predrilled holes (16-mm diameter). To facilitate their installation, these radial strain gages were first mounted onto epoxy sticks and then inserted into the predrilled holes. The holes were then filled with the same epoxy to achieve strain compatibility between the gage and the surrounding concrete. For

verification, a preliminary uniaxial compression test was conducted on a concrete cylinder which was instrumented with the embedded strain gages on-a-stick as well an external displacement transducer. The measured strains up to the onset of nonlinear behavior showed good agreement between the two methods. Note that subsequent test observation did not indicate any correlation between hole location and crack formation.

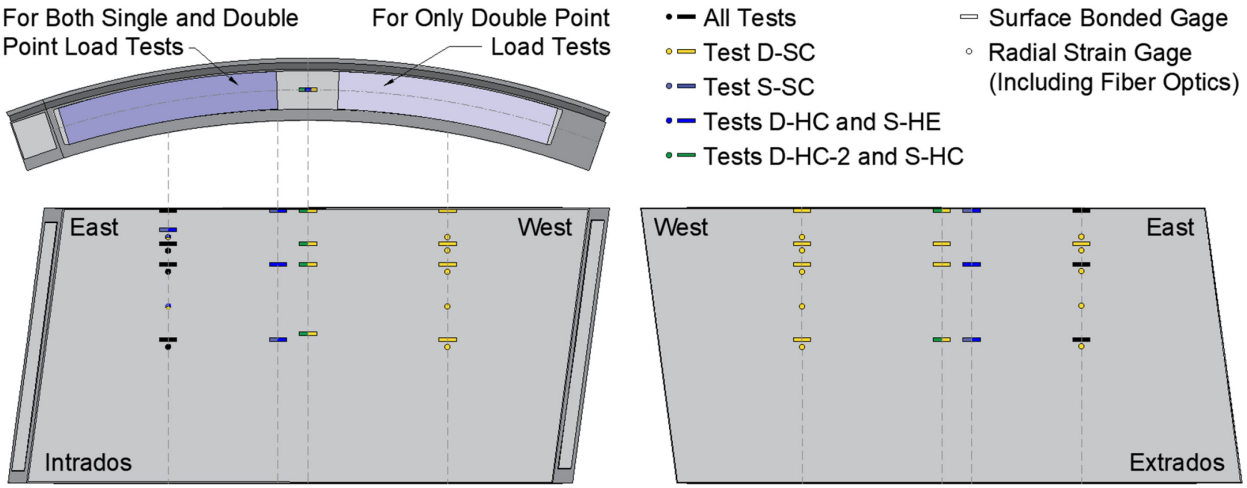

Figure 14: Strain gage layouts for all specimens

4. Results and Discussion

The thrust pad load-time histories of all six tests are plotted in Figure 15. The periodic stepwise pattern in these curves indicates a loading pause for crack observations. At pauses of loading, cracks were traced and labeled with the load level. Maximum crack widths were measured using a standard crack comparator card. Loading continued until either the full 22.2 MN capacity of the universal testing machine was applied or ultimate failure of the segment occurred due to a rapid loss of axial resistance. Four tests (D-SC, D-HC, S-HC, and S-HE) were able to withstand the full 22.2 MN capacity of the testing machine without reaching ultimate failure. The double pad load test on the hybrid-reinforced segment (D-HC-2) was stopped at an applied force level of 10.0 MN per pad (10% short of the maximum pad load in this setup) to minimize damage accumulation and enable a subsequent single pad load test (S-HC). Only the single pad load test

on the SFRC segment (S-SC) resulted in ultimate failure due to radial bursting prior to reaching the loading capacity of the testing machine.

The thrust jack load is also plotted in Figure 15 as a function of average displacement for each test, which represents the load-induced deformation from the top of the segment to the base plate (see Figure 11). For double pad tests, the displacement is averaged from the data collected by all four displacement transducers located on extrados and intrados faces under both loading pads (see Figure 13). For single pad tests, the displacement is averaged from the data collected by the two displacement transducers located on the extrados and intrados sides where thrust jack load is applied. The SFRC segment under double pad load (D-SC) exhibited higher stiffness in comparison with both tests on hybrid segments under the double pad load. This is likely attributed to the advanced age of 673 days (and associated curing gains in concrete stiffness) at testing, in comparison to the two hybrid segments which were aged 200 days at testing. The SFRC and hybrid segments under concentric single pad load exhibit similar trends in global load–deformation behavior. The hybrid segment under eccentric single pad loading (S-HE) exhibits a higher initial stiffness than the single pad concentric cases (S-HC and S-SC); however, the S-HE specimen softens at approximately 10 MN, after which its curve trends back to the other single pad specimens at higher loads.

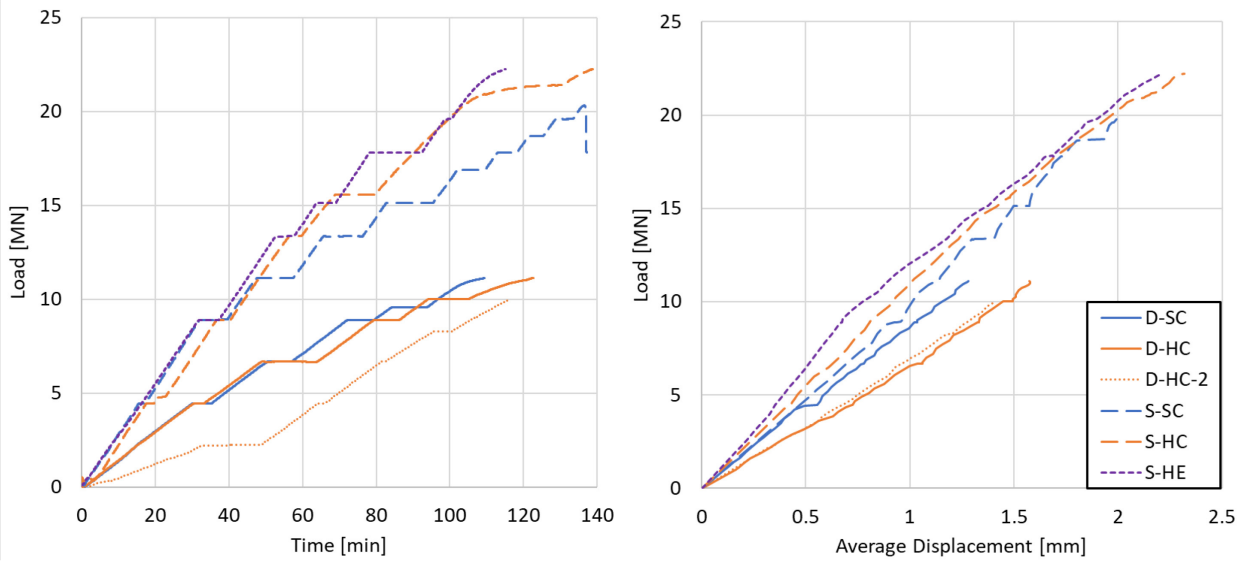

Figure 15: Thrust jack load histories for all tests: load per pad versus time (left), and load per pad versus average vertical displacement (right)

4.1. Serviceability Assessment (Double Pad Load Cases)

The performance of the segments under conventional double-pad thrust jack loading is assessed relative to the crack formation and strain measurements at the maximum expected thrust jack load during the construction of this particular tunnel (5.78 MN per pad) and at the maximum capacity of the TBM's jacking system (9.55 MN per pad). The crack markings on each specimen (made during the load stoppages in each test) were postprocessed to create a map of crack propagation with increasing load. Figure 16 presented a post-test, perspective-corrected crack propagation map for the intrados and extrados surfaces of each double pad loaded segment. Recall that crack widths were measured discretely at specific load levels; therefore, the lines between the pads do not represent crack growth but are used for illustrative purposes only. The cracks formed between each load stoppage are marked in Figure 16 with different colors. The largest number on the legend represents the maximum total applied thrust jack load during that test.

Each segment surface is divided into five regions to quantify the damage states. Regions A, B, D and E are correlated to transverse bursting crack formation, and region C correlates to spalling crack formation. Due to symmetry of loading on the double pad load tests, the crack size development of regions B/D and A/E are plotted together. The results from each segment are identified using the following descriptors: Double/Single pad load – Hybrid/SFRC Concentric/Eccentric – Intrados/Extrados – Cracking region. For example, D-HC-I-A represents the results from the **D**ouble pad load test on the **H**ybrid segment with **C**oncentric loading on the **I**ntrados face in region **A**. Note that crack sizes were not discretely measured on segment D-HC-2, and that specimen is therefore not included in the plots of crack width progression in Figure 16.

Overall, the crack maps of all three segments in Figure 16 show that the majority of cracking occurred once the pad load reached the 9.55 MN maximum TBM jacking capacity. Transverse spalling and bursting cracks were observed on the D-SC and D-HC segments, which were both taken up to 11.1 MN per pad. Transverse spalling cracks emerged in Region C between the load pads, initiating from the top or bottom of the segment and propagation towards the mid height. Transverse bursting cracks developed under the thrust jack pads

(primarily on the extrados face) and generally initiated under the load pad in the middle of the segment body and propagated towards the top and/or bottom.

A transverse spalling crack on the extrados face of segment D-HC formed first, between a load of 4.4 and 6.7 MN per pad. This was followed by the initiation of transverse bursting cracks between 6.7 and 8.9 MN per pad at the mid-height, and these cracks propagated at 10.0 MN per pad and eventually spanned from the top to bottom at a load of 11.1 MN. At the 9.55-MN maximum capacity of the TBM jacks, both transverse spalling and bursting cracks were observed but at widths below the AASHTO allowable limit of 0.2 mm. The transverse bursting crack size then exceeded the allowable limit of 0.2 mm between 10.0 and 11.1 MN per pad.

The D-HC-2 segment shows a relatively similar pattern and amount of cracking at the 10.0 MN per pad load level as the D-HC segment. The D-SC segment, on the other hand, shows a slightly delayed onset of cracking versus the D-HC segment. At the 5.78 MN maximum expected TBM load, no cracks were observed in the D-SC segment. The first D-SC transverse spalling crack forms at a load between 8.9 and 9.6 MN per pad, and the transverse bursting crack for that segment then emerges at a load between 9.6 and 11.1 MN per pad. The crack sizes in the D-SC segment remain below the 0.2 mm limit up to the maximum applied load of 11.1 MN per pad. Since only a few segments were tested, it is difficult to draw definitive conclusions about the differences in the onset of cracking between the SFRC and hybrid segments.

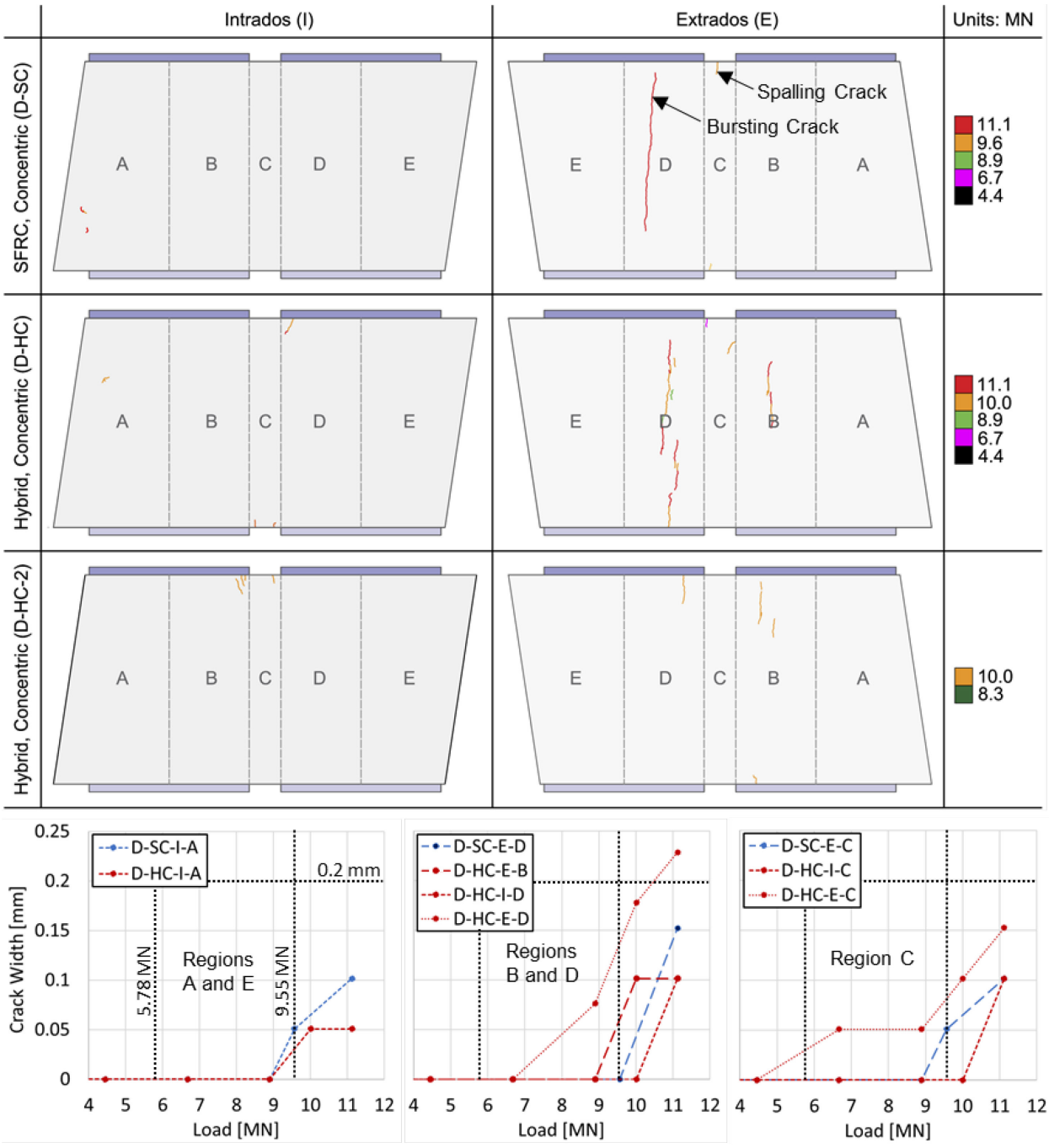

Figure 16: Crack propagation of double pad load tests: mapping on the intrados/extrados faces, and crack size plotted as a function of pad load

Figure 17 summarizes the tensile strain distribution as a function of load and location in these three regions for segments D-HC and D-SC. The figures are also shaded to illustrate the lower and upper bound tension strain limits. Specifically, the first green region indicates that strains are below the lower bound limit, the

second orange region is between the lower and upper bound limits, and third red region is above the upper bound limit. The strain development generally matches with the crack propagation shown in Figure 16.

In the D-SC segment (with SFRC only), the transverse spalling strains are highest near the top surface and decrease toward the mid height. Transverse bursting strains are largest at the mid height, and the radial bursting strains are largest near the load application at the top surface. The lower bound tension strain limit is first reached via transverse spalling at 4.4 MN per pad, followed by radial bursting between 4.4 and 5.6 MN, and then transverse bursting at 10.0 MN per pad. These load levels generally agree with the numerical predictions for the elastic and inelastic FE models summarized in Table 5. Furthermore, the measured locations of high strains correspond closely to the high strain regions illustrated in Figure 8 from the FE models. These results indicate that the elastic and inelastic FE models can provide an approximate, though slightly unconservative, estimate of damage formation in the tested segment.

The addition of conventional reinforcing bars in the hybrid D-HC segment makes a notable impact on strain development. As expected, Figure 17 shows that the measured transverse spalling strains near the top surface are reduced due to the presence of the embedded ladders of steel reinforcing bars. The radial bursting strains are also reduced in the elevated strain region near the top surface. At that location, the reinforcing bars themselves develop significant levels of strain, but the concrete strains are smaller compared to the SFRC-only segment. The development of transverse bursting strain under the load pads is not significantly impacted due to the fact that the reinforcing bars are at the edges of the segment and the highest strain region is near the middle of the segment. Transverse bursting strains are therefore similar in both the D-SC and D-HC segments.

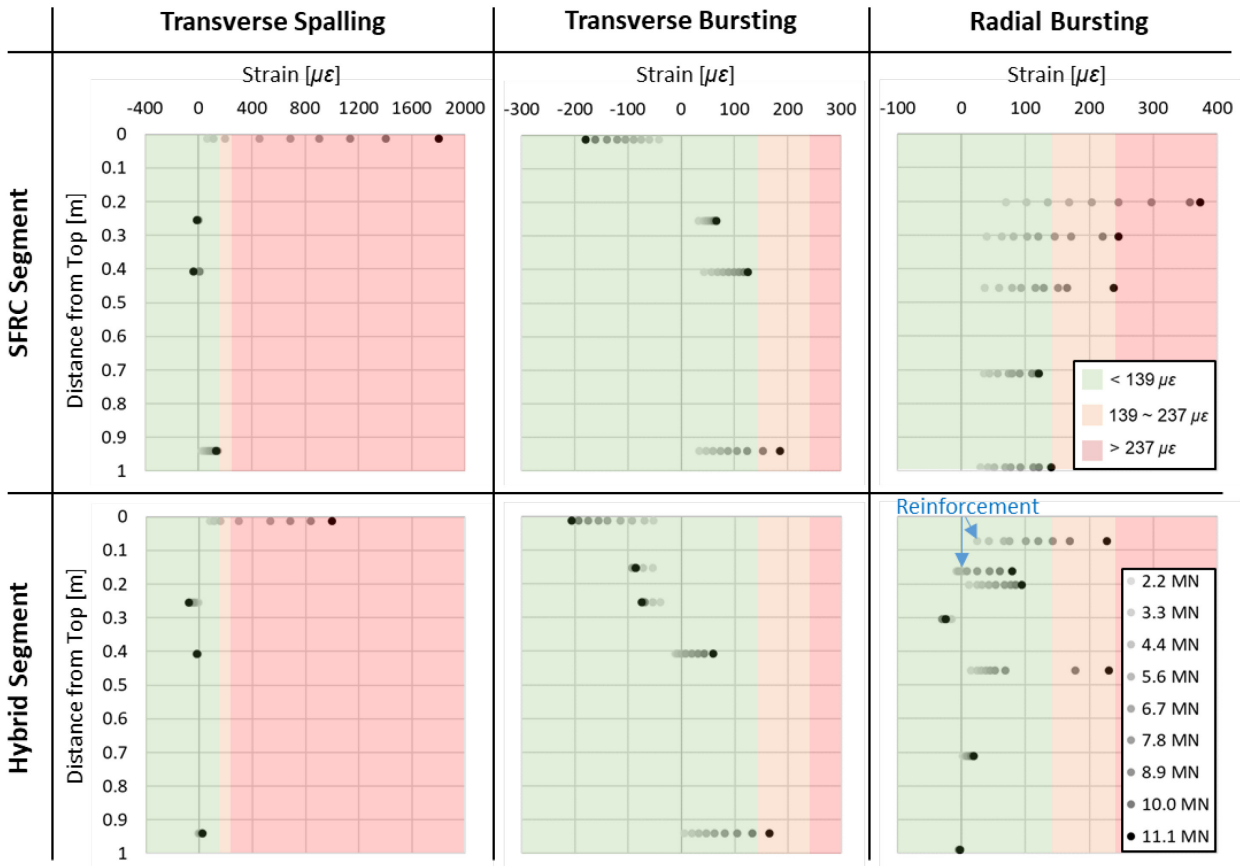

Figure 17: Distribution of strain development for double pad load segments D-HC and D-SC

Recall that the radial strain distributions were measured continuously through the thickness of segment D-SC using snaking fiber optic strain gages under both load pads. The resulting strain distributions as a function of load, distance from the extrados surface, and distance from the top surface are plotted in Figure 18. The radial strains are highest near the top surface at the load application and decreases with distance below the top surface. The strains under the east load pad tend to be marginally higher than at the west load pad. The strain at the top-most measurement (at 0.20 m from the top surface) exhibits a peak strain near the extrados surface at elevated loads, thus indicating radial crack formation. At this location, the largest radial strain is approximately ten times the tensile strain limit, indicating potential the onset of unobservable internal cracking. Based on the plots in Figure 18, the radial strains reached the tensile strain limits at a location 197 mm from the intrados surface and 0.2 m from the top surface. The lower limit of 139 με is reached at a load pad level of 3.7 MN per pad under the East load pad and at 6.2 MN under the West load

pad. The upper limit of 237 με is then reached at 6.2 MN per pad on the East side and 8.6 MN on the West side. This is marginally lower than the FE results, which reached the lower and upper bound tensile limits at 6.8 and 11.3 MN, respectively (see Table 5). Previous research by Iyengar indicates that the achievement of cracking at the lower load level may be attributed to non-uniform pressure distribution at the loaded pad in the experiment (Iyengar 1960). Overall, the radial strain distributions at the top level again compare reasonably well with those predicted by the FE models in Figure 8.

When subjected to relatively low thrust force (e.g. below 6.7 MN per pad), the radial strain distribution relatively uniform over the segment thickness. However, at higher loads (e.g. above 8.9 MN per pad), the radial strain distribution at 0.2 m below the top surface becomes increasingly nonuniform, and the maximum strain exceeds the maximum tensile strain limit of 237 $\mu\varepsilon$ at a pad load of 8.9 MN. At 11.1 MN per pad, the nonuniformity of radial strain distribution becomes even more significant, and the largest radial strain is now approximately 10 times beyond the strain limit, which suggests that the segment could become structurally compromised and lose axial stiffness via radial bursting with any further increase in thrust jack load. For comparison, the maximum transverse spalling strain at 11.1 MN per pad is still below the upper tensile strain limit of 237 $\mu\varepsilon$.

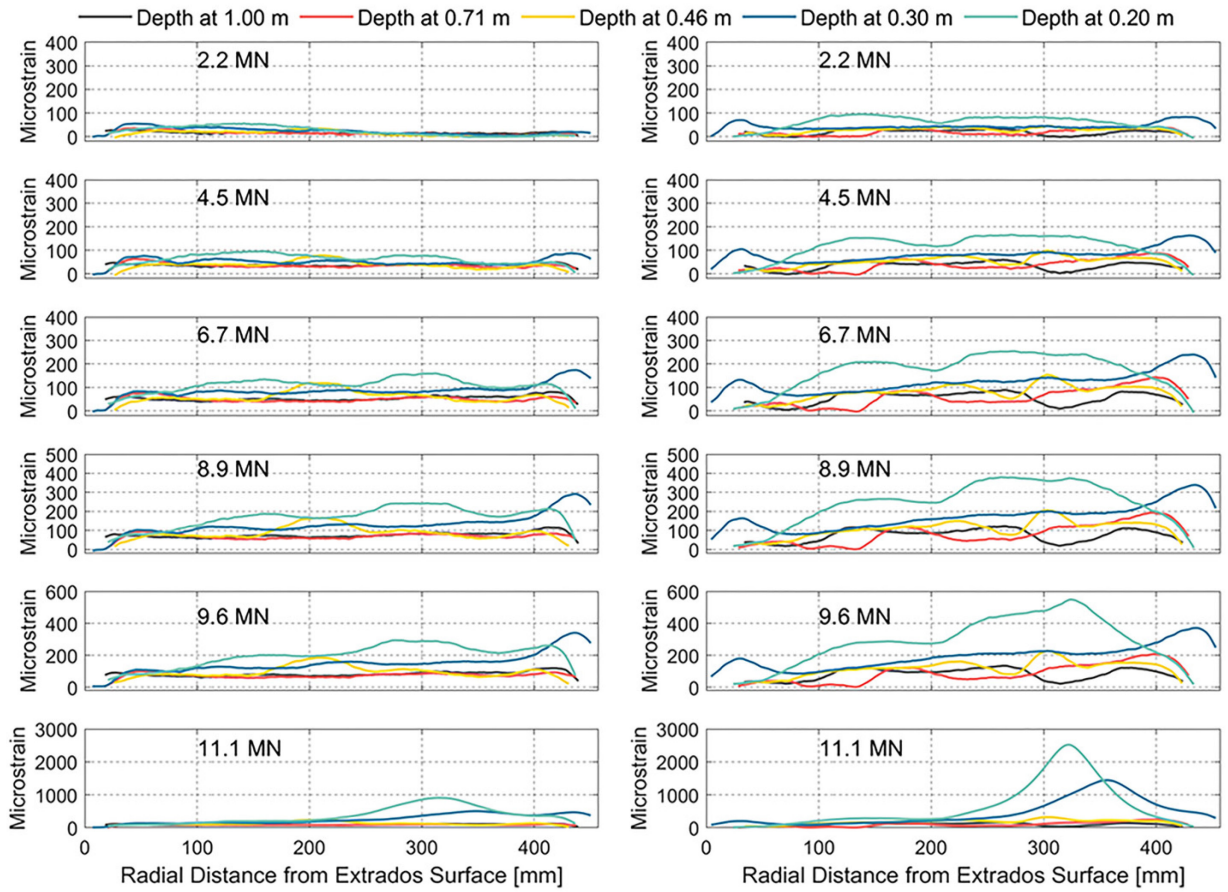

Figure 18: Radial strain evolution in the D-SC segment at under the west (left) and east (right) load pads

4.2. Ultimate Capacity Assessment (Single Pad Load Cases)

The double pad load tests showed that spalling stress caused the formation of initial cracks which do not propagate significantly; however, subsequent radial bursting stresses through the segment thickness can lead to increasingly significant cracking damage. Since the double pad loading setup could not progress any further to reach ultimate failure (due to the capacity of the universal testing machine), single pad load tests were conducted to investigate the governing damage modes at ultimate resistance to thrust jack loading. As shown previously in Table 6, the effects of supplementary conventional reinforcement and eccentricity were also investigated via three single pad load tests: a concentric pad load test on a SFRC segment (S-SC), a concentric pad load test on a hybrid reinforced segment (S-HC), and an eccentric pad load test (38 mm extrados) on the hybrid segment (S-HE). Recall that both single pad tests for hybrid segments were performed using specimens that had been tested previously under service-level double pad

loading: S-HC used the same segment as D-HC-2, and S-HE used the same segment as D-HC. As shown previously in Figure 16, tests D-HC and D-HC-2 produced only minor crack damage, and the specimens were therefore suitable for retesting under single pad loading.

The crack propagation of the three single pad load segments, including crack maps and crack width development plots, are shown in Figure 20. Each surface is divided into 3 regions, including 2 regions (A and B) under the load pad where bursting cracks form, and 1 region (C) outside of the load pad, where spalling cracks form. A noticeable difference in cracking damage becomes apparent at 13.3 MN, when transverse bursting crack formation in the SFRC segment becomes more pronounced (particularly in Region B) than that observed in either hybrid segment. Cracking in Region B for the SFRC segment shows a rapid subsequent increase at the pad load approaches 17 MN. The SFRC segment then experiences a distinct ultimate radial bursting stress failure at a single pad load magnitude of 20.3 MN, which is more than twice the maximum TBM jacking capacity of 9.55 MN per pad and almost four times the maximum expected thrust jack load per pad of 5.78 MN. The failure was abrupt, as the segment exhibited a sudden loss of axial stiffness (see Figure 15) in conjunction with significant splitting cracks (see Figure 19).

Neither hybrid segment exhibited any abrupt ultimate radial bursting stress failure, though significant cracks were observed after reaching the testing machine's maximum pad load of 22.2 MN as shown in Figure 20. Specifically, crack widths for both hybrid segments in Regions A and B under the pad load first exceeded the 0.2-mm AASHTO limit around 17 MN and reached a maximum width of 0.65 mm at the 22.2 MN maximum pad load. It can be inferred that the presence of reinforcement in the hybrid segments prevented an abrupt loss in strength after bursting crack formation. The 38-mm eccentricity towards the extrados surface for S-HE has no significant effect on cracking performance at this high load level. Though the supplemental reinforcement only minorly impacted the formation of cracks at service-level loads, the added bar ladders per Figure 5 (especially the radial tie-bars) appeared to provide additional resistance against ultimate failure due to radial bursting stresses.

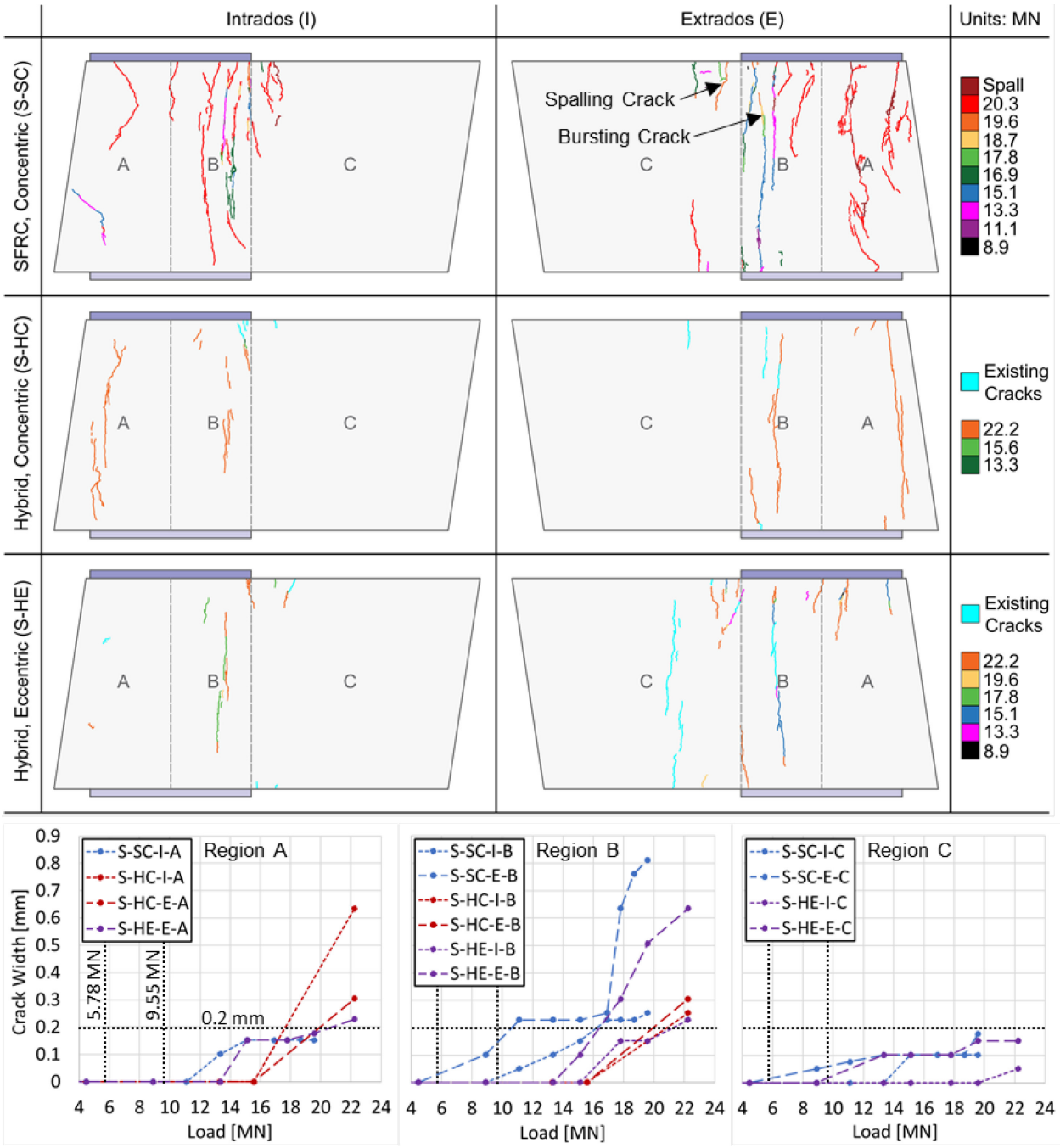

Figure 19: Crack propagation of single pad load tests: mapping on the intrados/extrados faces, and crack size plotted as a function of pad load

(a) (b) (c)

Figure 20: Crack damage following the single pad load test on SFRC segment S-SC: (a) failure induced by radial bursting stress, (b) concrete spall damage due to radial bursting, and (c) cracking caused by transverse bursting stress.

Figure 21 plots the bursting strain distributions from all single pad load tests. The largest transverse bursting strain generally develops under the load pad at segment mid-height, similar to the double pad load tests. Unfortunately, the radial strain measurements were not successful for the S-SC segment and are not presented. The SFRC and hybrid segments exhibit similar transverse strain distributions up to 13.3 MN, after which the hybrid segments undergo a more linear strain development while the SFRC segment exhibits a significant strain increase. Beyond 13.3 MN, the supplementary conventional reinforcement at the top face of the specimen under the load pad becomes increasing engaged in tension, as shown for the S-HE test. In comparison with test S-HC, the eccentric load in S-HE causes some changes in strain development on the intrados and extrados faces near the load pads. Specifically, the concentric S-HC test shows an increase of tension on the intrados surface and an increase in compression on the extrados surface as the pad load is increased. The opposite trend occurs for the S-HE test due to the eccentric bending moment.

Despite these variations within 0.2 m under the load pad, all three tests show relatively similar development of transverse bursting strain in Figure 21 at 0.4-1.0 m from the top surface toward mid-height. The only

major difference is that the S-HE test shows a sudden jump in intrados transverse bursting strain at 22.2 MN; however, post-test inspections suggested that this spike was caused by the development of a crack right at the strain gage location. These results suggest that the eccentric loading has relatively minor effect on strain development at locations further from the loaded face. Also, the accumulation of tensile strain in the hybrid segments' reinforcement near the loaded face helps mitigate cracking at these higher levels of loading.

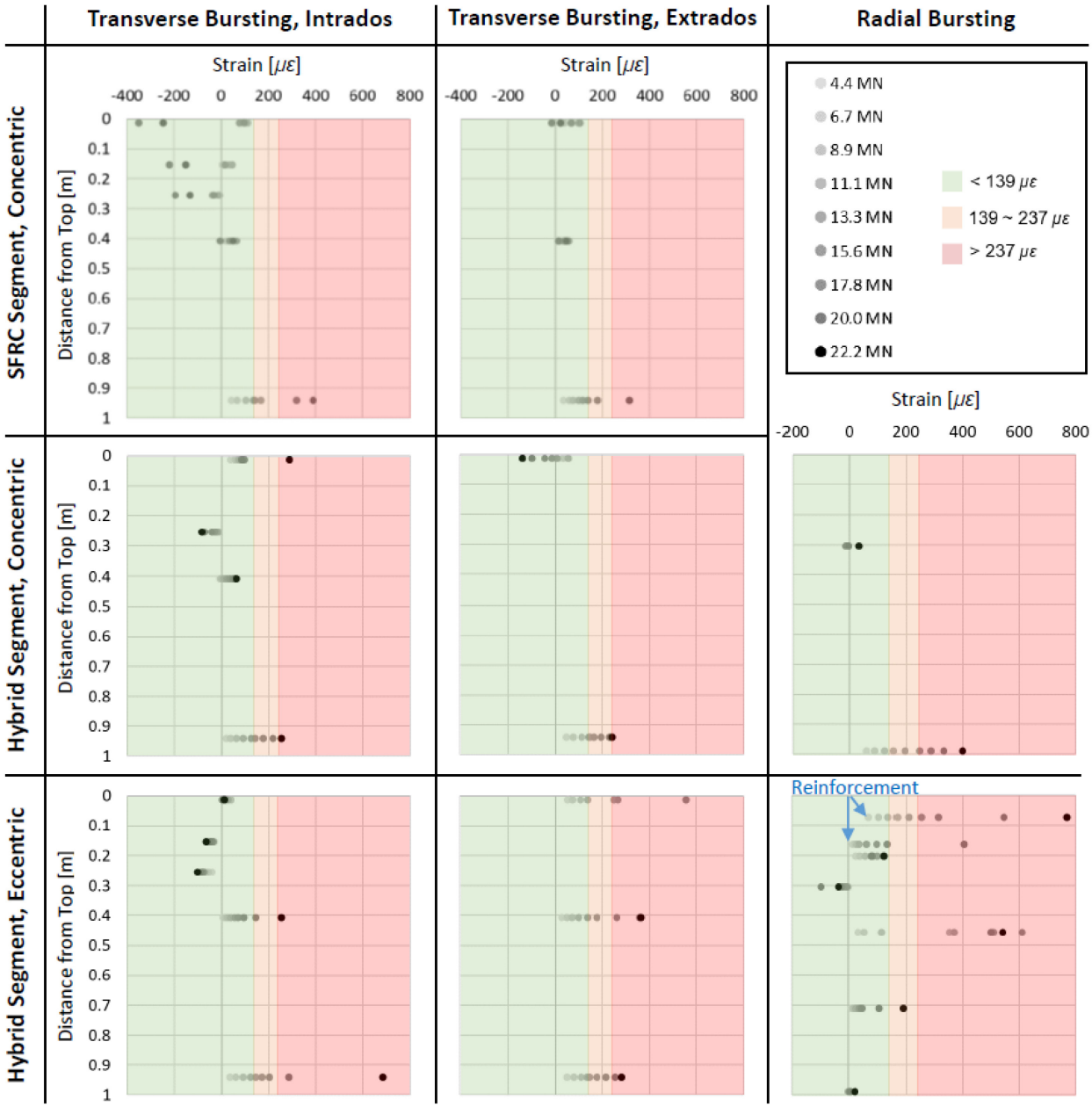

Figure 21: Distribution of strain development for single pad load tests

5. Conclusions

An experimental study was conducted to examine the response of full-scale PCTL segments to thrust jack loading. Two tests were performed on the segments fabricated with SFRC, and four tests were performed on hybrid segments fabricated with SFRC and supplemental steel bar reinforcement. Segments were loaded with a double pad load configuration to assess the performance under the maximum expected thrust jack load and the maximum jacking capacity of the TBM. Single pad load tests were conducted to examine the ultimate response of the segments, within the limitations of the testing machine. The following conclusions can be made based on the results of this test program:

- Observed crack propagation and strain measurements on the tested segments generally showed good agreement with expected crack formation from idealized design-basis FE analyses. Transverse spalling cracks form first, followed by high radial strains (indicative of radial cracking) and then by transverse bursting cracks.
- The elastic and nonlinear FE models both provide good predictions of the experimentally observed damage propagation. Due to the relative independence of the transverse spalling and bursting stresses as well as the overall size of the segments, the elastic model provides adequate accuracy in its prediction of first crack formation and subsequent tensile load limits at other locations. These results suggest that linear FE models can serve as a design-basis tool for evaluating a PCTL segment for thrust jack loading.
- The SFRC did not crack when subjected to the maximum expected thrust jack pad load level (5.78 MN per pad). Cracking did occur prior to the ultimate thrust jack pad load (9.55 MN per pad) of the TBM; however, crack sizes were generally less than the AASHTO design limit of 0.2 mm. The FE models conservatively predicted the onset of first cracking via transverse spalling for the SFRC segment.
- The SFRC segment reached an ultimate limit state at 20.3 MN in the single pad load test configuration via radial bursting failure. The onset of ultimate response was associated with a significant increase in large splitting cracks as well as a sudden loss of axial stiffness under thrust jack loading. This result indicates that the SFRC segment has a factor of safety greater than twice the maximum TBM jacking

capacity that was considered for this particular tunnel. The FE models also predicted the onset of radial bursting cracking at load pad levels that were comparable to those exhibited by the tested segments.

- The addition of supplemental reinforcement in the hybrid segments had only minor impact on the development of cracking at service load levels with the double pad test configuration. In fact, the hybrid segments under double pad loading first cracked via transverse spalling at a slightly lower pad load than the counterpart SFRC segment (most likely due to the placement of the reinforcing bars near the loaded surface). However, the supplemental reinforcement became increasingly engaged in tension at higher load levels toward the testing machine's 22.2 MN maximum per pad in the single load pad test configuration. As a result, the increased engagement of the reinforcing bars provided additional strength against bursting failure at ultimate load levels.
- Applying a radial thrust jack load eccentricity of 38 mm towards the extrados surface had some influence on strain development at measurement locations near the load pad, which was also reflected in FE simulations with similarly eccentric load configurations. However, the development of bursting strains at locations further from the loading pads showed little difference between eccentric and concentric configurations for both the tests and FE models.

The conclusions of this study provide tangible guidance for the design of PCTL segments to resist thrust jack loading; however, the following limitations should be noted:

- Strain measurements were generally taken at discrete locations, and peak strains may therefore exist at lower load levels in other regions of the segment. However, good overall agreement with the FE results indicates that this limitation would have negligible impact on the conclusions of testing.
- A stiff spreader beam was used to apply thrust jack load to the segments from the testing machine. Inherent flexibility in that beam likely introduced at least some non-uniform pressure on the double and single pad tests. Again, good overall agreement with the FE models (which applied the thrust jack load as an idealized uniform pressure over the pad area) somewhat mitigates the potential impact of this limitation.

- The tested and modeled segments were not restrained in the circumferential direction. In the actual tunnel, neighboring segments could provide restraining reactions in that direction, leading to some influence on strain development at those joint surfaces as well as throughout the body of the segment. Additional FE modeling should explore the potential impacts of additional restraint from a realistic panel-to-panel interfaces.

Acknowledgements

Financial support for the test program in this project has been provided by the U.S. Federal Highway Administration. Additional stipend and tuition support for graduate research assistant Ouyang was provided by the U.S. Department of Transportation (USDOT Grant #69A3551747118) via the University Transportation Center for Underground Transportation Infrastructure (UTC-UTI) at the Colorado School of Mines (CSM). Additional stipend support for undergraduate research assistant Patmanidis was provided by the Research Experience for Undergraduates in Underground Infrastructure, funded by the National Science Foundation (NSF Grant #1950487). The authors would also like to thank precast producer CSI for graciously donating all segments that were tested in this research program. The opinions expressed in this paper are the authors' and not the opinion of FHWA, the UTC-UTI, CSM, US DOT, NSF, or CSI.

References

AASHTO. 2017. *LRFD road tunnel design and construction guide specifications*. Washington, DC.: American Association of State Highway and Transportation Officials.

Abbas, S. 2014. "Structural and Durability Performance of Precast Segmental Tunnel Linings." Ph.D. Thesis. Canada: The University of Western Ontario.

Abrishambaf, A., J. A. O. Barros, and V. M. C. F. Cunha. 2015. "Tensile stress–crack width law for steel fibre reinforced self-compacting concrete obtained from indirect (splitting) tensile tests." *Cement and Concrete Composites*, 57: 153–165. https://doi.org/10.1016/j.cemconcomp.2014.12.010.

ACI Committee 318. 2019. *ACI 318-19: Building Code Requirements for Structural Concrete and Commentary*. Farmington Hills, MI: American Concrete Institute.

ACI Committee 544. 2016a. *ACI 544.7R-16 Report on Design and Construction of Fiber-Reinforced Precast Concrete Tunnel Segments*. Farmington Hills, MI: American Concrete Institute.

ACI Committee 544. 2016b. *ACI 544.8R-16 Report on indirect method to obtain stress-strain response of fiber-reinforced concrete (FRC)*. Farmington Hills, Mich.: American Concrete Institute.

ASTM Standard A615-18. 2018. *Specification for Deformed and Plain Carbon-Steel Bars for Concrete Reinforcement*. West Conshohocken, PA: ASTM International.

ASTM Standard A820-16. 2016. *Specification for Steel Fibers for Fiber-Reinforced Concrete*. West Conshohocken, PA: ASTM International.

ASTM Standard C39-20. 2020. *Test Method for Compressive Strength of Cylindrical Concrete Specimens*. West Conshohocken, PA: ASTM International.

ASTM Standard C469-14. 2014. *Standard Test Method for Static Modulus of Elasticity and Poisson's Ratio of Concrete in Compression*. West Conshohocken, PA: ASTM International.

ASTM Standard C496-17. 2017. *Test Method for Splitting Tensile Strength of Cylindrical Concrete Specimens*. West Conshohocken, PA: ASTM International.

Bakhshi, M., and V. Nasri. 2014. "Design considerations for precast tunnel segments according to international recommendations, guidelines and standards." 9. Vancouver Canada: Tunnelling Association of Canada.

Barros, J. A. O., V. M. C. F. Cunha, A. F. Riberiro, and Antunes. 2004. "Post-cracking behaviour of steel fibre reinforced concrete." *Mater. Struct.*, 38 (275): 47–56. https://doi.org/10.1617/14058.

Beňo, J., and M. Hilar. 2013. "Steel Fibre Reinforced Concrete for Tunnel Lining – Verification by Extensive Laboratory Testing and Numerical Modelling." *Acta Polytech*, 53 (4). https://doi.org/10.14311/1823.

Breen, J. E., O. Burdet, C. Roberts, D. Sanders, and G. Wollmann (Eds.). 1994. *Anchorage zone reinforcement for post-tensioned concrete girders*. Report / National Cooperative Highway Research Program. Washington, D.C: Transportation Research Board, National Research Council : National Academy Press.

Burgers, R., J. Walraven, G. A. Plizzari, and G. Tiberti. 2007. "Structural behavior of SFRC tunnel segments during TBM operations." *World Tunnel Congress ITA-AITES*, 1461–1467.

Caratelli, A., A. Meda, Z. Rinaldi, and P. Romualdi. 2011. "Structural behaviour of precast tunnel segments in fiber reinforced concrete." *Tunnelling and Underground Space Technology*, 26 (2): 284–291. https://doi.org/10.1016/j.tust.2010.10.003.

CEN. 2005. *Test method for metallic fibered concrete - Measuring the flexural tensile strength*. Brussels, Belgium: European Committee for Standardization.

CEN. 2006. *Fibres for concrete - Part 1: Steel fibres - Definitions, specifications and conformity*. Brussels, Belgium: European Committee for Standardization.

Conforti, A., G. Tiberti, and G. A. Plizzari. 2016. "Combined effect of high concentrated loads exerted by TBM hydraulic jacks." *Magazine of Concrete Research*, 68 (21): 1122–1132. https://doi.org/10.1680/jmacr.15.00430.

Conforti, A., G. Tiberti, G. A. Plizzari, A. Caratelli, and A. Meda. 2017. "Precast tunnel segments reinforced by macro-synthetic fibers." *Tunnelling and Underground Space Technology*, 63: 1–11. https://doi.org/10.1016/j.tust.2016.12.005.

Conforti, A., I. Trabucchi, G. Tiberti, G. A. Plizzari, A. Caratelli, and A. Meda. 2019. "Precast tunnel segments for metro tunnel lining: A hybrid reinforcement solution using macro-synthetic fibers." *Engineering Structures*, 199: 109628. https://doi.org/10.1016/j.engstruct.2019.109628.

Dassault Systèmes. 2019. "Abaqus/CAE 2020." Johnston, RI, USA: Dassault Systemes Simulia Corp.

German Tunnelling Committee. 2013. *Recommendations for the design, production and installation of segmental rings*. Cologne, Germany: DAUB.

Graybeal, B., and F. Baby. 2013. "Development of Direct Tension Test Method for Ultra-High-Performance Fiber-Reinforced Concrete." *ACI Materials Journal*, (110): 177–186. https://doi.org/10.14359/51685532.

Groeneweg, T. 2007. "Shield Driven Tunnels in Ultra High Strength Concrete - Reduction of the Tunnel Lining Thickness." PhD Thesis. Delft University of Technology.

Hilar, M., J. L. Vitek, and R. Pukl. 2012. "Laboratory Testing and Numerical Modelling of Sfrc Tunnel Segments." *Eastern European Tunnelling Congress*. Budapest, Hungary.

International Federation for Structural Concrete. 2013. *fib Model Code for Concrete Structures 2010*. Bulletin / Fédération Internationale du Béton. Lausanne, Switzerland: International Federation for Structural Concrete (fib).

ISO. 2013. *ISO 13270:2013 Steel fibres for concrete — Definitions and specifications*. International Organization for Standardization.

ITA Working Group 2. 2019. *Guidelines for the design of segmental Tunnel Linings*. 59. Longrine, France: International Tunnelling Association.

Iyengar, K. T. S. R. 1960. "Der Spannungszustand in Einem Elastischen Halbstreifen Und Seine Technischen Anwendungen." Dissertation. Hannover: Technische Hochschule.

Iyengar, K. T. S. R. 1962. "Two-Dimensional Theories of Anchorage Zone Stresses in Post-Tensioned Prestressed Beams." *JP*, 59 (10): 1443–1466. https://doi.org/10.14359/7961.

Krahl, P. A., I. I. Palomo, S. J. de C. Almeida, G. Henrique Siqueira, N. de O. Pinto Júnior, and L. C. M. Vieira Junior. 2021. "Tolerances for TBM thrust load based on crack opening performance of fiber-reinforced precast tunnel segments." *Tunnelling and Underground Space Technology*, 111: 103847. https://doi.org/10.1016/j.tust.2021.103847.

Nogales, A., and A. de la Fuente. 2020. "Crack width design approach for fibre reinforced concrete tunnel segments for TBM thrust loads." *Tunnelling and Underground Space Technology*, 98: 103342. https://doi.org/10.1016/j.tust.2020.103342.

Olesen, J. F. 2001. "Fictitious Crack Propagation in Fiber-Reinforced Concrete Beams." *J. Eng. Mech.*, 127 (3): 272–280. https://doi.org/10.1061/(ASCE)0733-9399(2001)127:3(272).

RILEM TC 162-TDF. 2003. "Final Recommendation of RILEM TC 162-TDF: Test and Design Methods for Steel Fibre Reinforced Concrete: σ-ε Design Method." *Materials and Structures*, 36.

Shen, Q., W. Chen, C. Liu, W. Zou, and L. Pan. 2020. "The Tensile Strength and Damage Characteristic of Two Types of Concrete and Their Interface." *Materials*, 13 (1): 16. Multidisciplinary Digital Publishing Institute. https://doi.org/10.3390/ma13010016.

Stephen, S. J., B. Raphael, R. Gettu, and S. Jose. 2019. "Determination of the tensile constitutive relations of fiber reinforced concrete using inverse analysis." *Construction and Building Materials*, 195: 405–414. https://doi.org/10.1016/j.conbuildmat.2018.11.014.

Trabucchi, I., G. Tiberti, and G. A. Plizzari. 2021. "A parametric numerical study on the behavior of large precast tunnel segments during TBM thrust phase." *Engineering Structures*, 241: 112253. https://doi.org/10.1016/j.engstruct.2021.112253.

Winterberg, R., and T. Clarke. 2021. "Performance of Tunnel Segments Reinforced with Synthetic Macro Fibers." *Proceedings of the World Tunnel Congress*, 837–853. Society for Mining, Metallurgy & Exploration.